

## **The role of bed roughness in wave transformation across sloping rock shore platforms**

Poate, Timothy G.; Masselink, G.; Austin, Martin; Dickson, Mark; McCall, Robert T.

**Journal of Geophysical Research: Earth Surface**

DOI:  
[10.1002/2017JF004277](https://doi.org/10.1002/2017JF004277)

Published: 01/01/2018

Peer reviewed version

[Cyswllt i'r cyhoeddiad / Link to publication](#)

*Dyfyniad o'r fersiwn a gyhoeddwyd / Citation for published version (APA):*

Poate, T. G., Masselink, G., Austin, M., Dickson, M., & McCall, R. T. (2018). The role of bed roughness in wave transformation across sloping rock shore platforms. *Journal of Geophysical Research: Earth Surface*, 123(1), 97-123. <https://doi.org/10.1002/2017JF004277>

### **Hawliau Cyffredinol / General rights**

Copyright and moral rights for the publications made accessible in the public portal are retained by the authors and/or other copyright owners and it is a condition of accessing publications that users recognise and abide by the legal requirements associated with these rights.

- Users may download and print one copy of any publication from the public portal for the purpose of private study or research.
- You may not further distribute the material or use it for any profit-making activity or commercial gain
- You may freely distribute the URL identifying the publication in the public portal ?

### **Take down policy**

If you believe that this document breaches copyright please contact us providing details, and we will remove access to the work immediately and investigate your claim.



## THE ROLE OF BED ROUGHNESS IN WAVE TRANSFORMATION ACROSS SLOPING ROCK SHORE PLATFORMS

*Tim Poate*<sup>1</sup>, *Gerd Masselink*<sup>1</sup>, *Martin J. Austin*<sup>2</sup>, *Mark Dickson*<sup>3</sup>, *Robert McCall*<sup>4</sup>

<sup>1</sup> School of Biological and Marine Sciences, Plymouth University, Drake Circus, Plymouth, PL4 8AA, UK

<sup>2</sup> School of Ocean Sciences, Bangor University, Menai Bridge, Anglesey, LL59 5AB, UK

<sup>3</sup> School of Environment, The University of Auckland, Auckland 1142, New Zealand

<sup>4</sup> Department of Marine and Coastal Systems, Deltares, Boussinesqweg 1, 2629 HV Delft, the Netherlands

Corresponding author: Tim Poate (timothy.poate@plymouth.ac.uk)

### Key Points:

- Extensive field dataset and numerical simulations exploring bed roughness on wave transformation
- Bed roughness not significant in the surf zone; therefore, friction can be neglected for short wave transformation on rocky platforms
- In model simulations, friction is only significant outside of the surf zone for very rough flat platforms and during small wave conditions.

## Abstract

We present for the first time observations and model simulations of wave transformation across sloping (Type A) rock shore platforms. Pressure measurements of the water surface elevation using up to 15 sensors across five rock platforms with contrasting roughness, gradient and wave climate, represent the most extensive collected, both in terms of the range of environmental conditions, and the temporal and spatial resolution. Platforms are shown to dissipate both incident and infragravity wave energy as skewness and asymmetry develop and, in line with previous studies, surf zone wave heights are saturated and strongly tidally-modulated. Overall, the observed properties of the waves and formulations derived from sandy beaches does not highlight any systematic inter-platform variation, in spite of significant differences in platform roughness, suggesting that friction can be neglected when studying short wave transformation. Optimisation of a numerical wave transformation model shows that the wave breaker criterion falls between the range of values reported for flat sandy beaches and those of steep coral fore-reefs. However, the optimised drag coefficient shows significant scatter for the roughest sites and an alternative empirical drag model, based on the platform roughness, does not improve model performance. Thus, model results indicate that the parameterisation of frictional drag using the bottom roughness length-scale may be inappropriate for the roughest platforms. Based on these results, we examine the balance of wave breaking to frictional dissipation for rock platforms and find that friction is only significant for very rough, flat platforms during small wave conditions outside the surf zone.

## 1. Introduction

One of the longest standing debates in rocky coast geomorphology is whether subaerial weathering or wave processes dominate shore platform evolution (Kennedy et al., 2011), i.e., the ‘wave versus weathering debate’. One approach to help resolve this issue is through the measurement of surf zone hydrodynamics to quantify wave energy dissipation, wave forces and wave-driven currents across shore platforms. For example, Stephenson and Kirk (2000) made wave height measurements across a quasi-horizontal platform in New Zealand and found that, despite the energetic offshore wave conditions, the amount of energy delivered to the platforms was very low with only 5 – 7 % of the wave energy at the seaward edge of the platform reaching the cliff foot; they concluded that wave erosion was not effective in this area. The quantification of wave energy levels across the shore platform is also relevant in assessing the delivery of wave energy to the cliff toe (Naylor et al., 2010), and for determining the likelihood of large boulders being moved by waves across the platform (Nott, 2003).

Shore platforms are (quasi-) horizontal or gently-sloping rock surfaces, generally centred around MSL and extending between spring high and spring low tidal level (Kennedy, 2015). They are abundant along energetic rocky coasts and are often backed by eroding cliffs, sometimes with a beach deposit present at the cliff-platform junction. The development of shore platforms is intrinsically linked to coastal cliff erosion (Trenhaile, 1987), and they have been described as erosional stumps left behind by a retreating sea cliff (Pethick, 1984).. Two shore platform types have been described (Sunamura, 1992): Type A platforms are characterised by a gently-sloping ( $\tan\beta = 0.01 - 0.05$ ) surface that extends beneath sea level without a marked break in slope, and are usually found in large tidal environments (mean spring tide range  $> 2$  m); Type B platforms are characterised by a (quasi-)

horizontal surface fronted by a steep scarp (sometimes referred to as a low tide cliff) and typically occur in small tidal settings (mean spring tide range < 2 m).

Measurements have shown that shore platform gradient is positively correlated with tidal range (Trenhaile, 1999); however, it has recently been suggested that platform gradient may also be affected by the sea-level history (Dickson and Pentney 2012). The shore platform surface depends mainly on geological factors, such as lithology and the characteristics of the stratigraphic beds (thickness, strike, slip, etc.), and ranges from very smooth (similar to a sandy beach) to very rough (similar to a coral reef edge) (Trenhaile, 1987). Both the gradient and the roughness of shore platforms are expected to play key roles in driving nearshore dynamics through their effect on wave transformation processes, incident wave energy decay, wave set-up and infragravity wave generation.

Despite the recognised importance of wave processes in influencing shore platform dynamics and evolution (e.g., Dickson et al., 2013; Kennedy and Milkins, 2014), there is a paucity of appropriate process measurements made in these settings and even fewer studies in macrotidal environments. This represents a considerable time lag compared to nearshore research on sandy beaches, where wave data have been routinely collected since the 1980s (cf. Komar, 1998), and also compared to investigations of wave transformation process across coral reef platform (e.g., Brander et al., 2004; Lowe et al., 2005). The latter are rather similar to rocky shore platforms, both in terms of the gentle gradient (especially the Type B platforms) and the rough surface. Long term evolution of platforms has been addressed by Dickson et al., (2013) who challenges simplified steady-state equilibrium models that apply exponential decay, in wave height, and do not consider infragravity wave frequencies. This work links with that of Kennedy and Milkins, (2014) who address beach accumulation on platforms as a possible negative feedback to reduce cliff-retreat through increase wave dissipation.

A limited number of field data sets are available describing wave transformation across rocky shore platforms in micro-tidal settings. A common feature of these studies is the tidal modulation of the wave height and the depth limitation of the surf zone wave heights across the platform (Farrell et al., 2009; Marshall and Stephenson, 2011; Ogawa et al., 2011, 2015, 2016). The concept of a ‘saturated surf zone’ (Thornton and Guza, 1982) is well-demonstrated in each of these field investigations and concurrent with the dissipation of short-wave energy is the increase in the infragravity wave height (Beetham and Kench, 2011; Ogawa et al., 2015). The latter finding is potentially a very important geomorphic process, especially during energetic wave conditions (storms), because it is these waves that may dominate the water motion at the landward edge of the shore platform and provide the main force for cliff erosion and cliff-toe debris removal (Dickson et al., 2013).

A useful parameterisation of the wave conditions in the surf zone is the ratio of wave height  $H$  to water depth  $h$ . For mono-chromatic waves, this parameter is referred to as the breaker index  $\gamma$  and its value ranges from about 0.7 to 1.2. For random waves,  $H/h$  must be defined in statistical terms and usually the root-mean-square wave height  $H_{rms}$  or the significant wave height  $H_s$  is used. For consistency, all  $H/h$  values quoted in this paper are  $H_s/h$ , and values in the literature based on  $H_{rms}$  have been converted to  $H_s/h$  using  $H_s = \sqrt{2}H_{rms}$ . Original work on sandy beaches by Thornton and Guza (1982) suggested that  $H_s/h$  is constant in the surf zone with an upper-bound value of  $H_s/h = 0.59$ , and this value has also been found in subsequent work (Wright et al., 1982; King et al., 1990). However, field and laboratory studies of wave transformation processes have also found that  $H_s/h$  depends on wave steepness (Nairn, 1990), cross-shore position (Vincent, 1985) and beach gradient

(Sallenger and Holman, 1985; Masselink and Hegge, 1995). In particular, the latter dependency on beach gradient is relevant for shore platforms: for example, assuming  $\tan\beta = 0$  for a Type B platform and  $\tan\beta = 0.03$  for a Type A platform results in a value for  $H_s/h$  of 0.42 and 0.56, respectively, according to Sallenger and Holman (1985), and 0.5 and 0.65, respectively, according to Masselink and Hegge (1995). Based on field observations from three sandy beaches, Raubenheimer et al. (1996) proposed the following equation that predicts  $H_s/h$  as a function of beach gradient  $\tan\beta$ , water depth  $h$  and wave number  $k$ :

$$\frac{H_s}{h} = 0.19 + 1.05 \frac{\tan\beta}{kh} \quad \text{Eq. (1)}$$

where  $k$  is the local wave number given by  $2\pi/L$ , and where the wave length  $L$  is computed based on the wave period derived from the incident-wave centroidal frequency. Care should be taken when comparing  $H_s/h$  values between different studies due to the variety in methods used to derive  $H_s$  from data (e.g., measurements based on wave staffs, pressure sensors and current meters; use of different high- and low-frequency cut-offs, different methods for correcting for linear depth attenuation); for example, Raubenheimer et al. (1996) uses a high-frequency cut-off of 0.18 Hz and does not correct the remaining water level signal for depth attenuation. Additionally,  $H_s/h$  is also likely to depend on offshore bathymetry that is not accounted for in the simple  $\tan\beta/kh$  parameterisation, e.g., the presence of a sand bar.

Previous work on shore platforms has suggested values for  $H_s/h$  of 0.59 (Farrell et al., 2009), 0.4 (Ogawa et al., 2011) and 0.4 – 0.6 (Ogawa et al., 2015; depending on platform gradient). It is noted that these  $H_s/h$  values are upper-bound values and not the result of least-squares analysis between  $H_s$  and  $h$  for saturated surf zone conditions, such as was carried out to derive Eq. (1). The notion of identifying an upper-bound value for  $H_s/h$  stems from wave transformation studies across coral reef platform where the aim is to identify the maximum wave condition that can occur for a given water depth over the reef (e.g., Nelson, 1994; Hardy and Young, 1996). The parameter  $H_s/h$  is useful for making an assessment of wave conditions as a function of water depth. For example, if  $H_s/h$  across a shore platform is 0.5 and the water depth  $h$  at the landward extent of the platform and at the base of the cliff is 2 m, then the waves impacting on the cliff are characterised by a significant wave height  $H_s$  of 1 m. More specifically, however,  $H_s/h$  is related to the rate of incident wave energy dissipation in the surf zone, which in turn controls radiation stress gradients, wave set-up and nearshore currents.

The ability to model the transformation of waves across the surf zone is clearly important, whether the surf zone is on a sandy beach or a rocky shore platform. Analytical and numerical models use the breaker index  $\gamma_s$  as an essential tuning/calibration parameter for computing surf zone wave transformation and breaker-induced wave height decay (see Section 2). It has been established that  $H_s/h$  is strongly dependent on the bed gradient  $\tan\beta$  (Sallenger and Holman, 1985; Masselink and Hegge, 1995; Raubenheimer et al., 1996) and that steep surfaces are characterised by larger  $H_s/h$  values than gently-sloping surfaces. What is unknown, however, is whether the roughness of the surface over which the surf zone waves propagate plays a role in the wave transformation process and directly affects the value of  $\gamma_s$  used in these models. According to Kobayashi and Wurjanto (1992), incident wave energy dissipation due to bottom friction is negligible in the surf zone of sandy beaches; however, Lowe et al. (2005) found that at the front of a coral reef, energy dissipation by bottom friction was comparable to that by wave breaking under modal wave conditions, and even exceeded breaking-induced dissipation under low wave conditions. These conflicting findings are easily

explained by the vastly different bed roughness values between sandy beaches and coral reefs. In terms of bed roughness, shore platforms can range from beaches to coral reefs, with their surfaces ranging from extremely smooth to extremely rough, and with vertical variability varying from several millimetres to up to a meter.

The aim of this paper is to investigate whether wave transformation processes on shore platforms are different from that on sandy beaches due to differences in bed roughness. Specifically, we hypothesise that rough shore platforms enhance incident wave dissipation by friction (as opposed to breaking) and may influence energy transfer to the infragravity band by changing wave energy gradients in the surf zone and lowering incident-band wave heights in the shoaling zone. The hypothesis will be tested by comparing  $H_s/h$ , as well as the amount of infragravity wave energy across five different shore platforms representing a range of bed roughness values and gradients, and comparing these values with those obtained from a sandy beach. The simple wave transformation model developed by Thornton and Guza (1983) will be used to help interpret and complement the field results, and is introduced and discussed in Section 2. The field sites and the methodology used to collect and analyse the data are described in Section 3. The results obtained in the field and derived from a numerical model are presented in Section 4 and 5, respectively, and the implications are discussed in Section 6.

## 2. Modelling wave transformation

The wave height across a mildly-sloping nearshore, whether a beach or a shore platform, can be predicted using the wave height transformation model of Thornton and Guza (1983), which is an extension of the earlier model of Battjes and Janssen (1978). Assuming straight and parallel contours, the energy flux balance is:

$$\frac{\partial EC_g}{\partial x} = -\langle \varepsilon_b \rangle - \langle \varepsilon_f \rangle \quad \text{Eq. (2)}$$

where  $E$  is the energy density,  $C_g$  is the wave group velocity,  $x$  is the cross-shore coordinate,  $\langle \varepsilon_b \rangle$  is breaker dissipation and  $\langle \varepsilon_f \rangle$  is dissipation due to bed friction. The energy density and group velocity are calculated using the linear wave theory relationships:

$$E = \frac{1}{8} \rho g H_{rms}^2 \quad \text{Eq. (3)}$$

$$C_g = \frac{c}{2} \left( 1 + \frac{2kh}{\sinh 2kh} \right) \quad \text{Eq. (4)}$$

where  $\rho$  is the density of sea water,  $g$  is the gravitational acceleration,  $H_{rms}$  is the root mean square wave height,  $k$  is the wave number corresponding to the peak frequency  $f_p$  of the wave spectrum and  $h$  is the local water depth. Thornton and Guza (1983) parameterise the rate of dissipation due to wave breaking as:

$$\langle \varepsilon_b \rangle = \frac{3\sqrt{\pi}}{16} \rho g B^3 f_p \frac{H_{rms}^5}{\gamma^2 h^3} \left[ 1 - \frac{1}{(1 + (H_{rms}/\gamma h)^2)^{5/2}} \right] \quad \text{Eq. (5)}$$

where  $B$  is an empirical breaker coefficient  $O(1)$  for the case of fully developed bores (Thornton and Guza, 1982) and  $\gamma$  is the critical wave breaking parameter. The rate of dissipation due to bottom

friction is calculated by Thornton and Guza (1983) assuming quadratic bottom shear stress and parameterised as:

$$\langle \varepsilon_f \rangle = \rho C_f \frac{1}{16\sqrt{\pi}} \left[ \frac{2\pi f_p H_{rms}}{\sinh kh} \right]^3 \quad \text{Eq. (6)}$$

where  $C_f$  is the bottom drag coefficient.

The energy flux balance equation **Eq. (2)** is solved by substitution of the breaking wave dissipation **Eq. (5)** and bottom friction dissipation **Eq. (6)** functions, and numerically integrating over the cross-shore spatial domain using a simple forward-stepping scheme, where

$$EC_g|_2 = EC_g|_1 + \langle \varepsilon_b \rangle|_1 \Delta x + \langle \varepsilon_f \rangle|_1 \Delta x \quad \text{Eq. (7)}$$

Starting from the offshore boundary (location 1), where  $H_{rms,1}$  and  $f_p$  are known, the predicted quantities are obtained via **Eq. (7)**.  $C_{gs,1,2}$  and  $E_1$  are computed using linear theory (**Eqs. (3)** and **(4)**) and the known values of  $H_{rms,1}$ , and  $h_1$  and  $h_2$ . The rates of breaking wave and frictional dissipation (**Eqs. (5)** and **(6)**) are calculated, and  $E_2$  and therefore  $H_{rms,2}$  are then predicted.

The breaker coefficient  $B$  is generally taken as a constant ( $B = 1$ ; e.g., Lowe et al., 2005); therefore, the wave height transformation according to the Thornton and Guza (1982) model is only determined by the two ‘free’ parameters  $\gamma$  and  $C_f$ , which, respectively, control the rate of dissipation through breaking and bottom friction. It is informative to analyse the effect of these parameters on wave transformation over a plane-sloping bed. Figure 1 shows the results of a number of simulations using **Eq. (7)** and a range of  $\gamma$  and  $C_f$  spanning values reported in the literature. The boundary conditions for the model runs are characterised by  $H_o = 0.6$  m,  $T_p = 7.5$  s and  $\tan\beta = 0.02$ . Eight simulations were run with  $C_f$  fixed at 0.01 and  $\gamma$  varied from 0.35 to 0.7 (in 0.05 increments); the other eight simulations were run with  $\gamma$  held constant at 0.42 and  $C_f$  varied from 0.01 to 0.15 (in 0.02 increments).

Wave energy dissipation by breaking, parameterised by  $\gamma$ , exerts a strong control on the wave height transformation. Increasing  $\gamma$  allows larger waves to propagate and shoal closer to the shoreline before breaking. This increases the rate of breaker dissipation across a narrow cross-shore region and causes larger values of the local wave height to water depth ratio  $H/h$ . Wave energy dissipation by bed friction is controlled by the bed roughness, parameterised by a drag coefficient  $C_f$ . Increasing  $C_f$  enhances energy dissipation and opposes the increase in wave height during the shoaling process. Energy dissipation due to friction is generally less than by wave breaking, even for the largest  $C_f$  values, and is mainly observed outside the surf zone. There is a weak influence of  $C_f$  on the local  $H/h$  with the largest  $H/h$  values associated with the smoothest bed (smallest  $C_f$ ). Overall, these model results suggest that  $\gamma$  exerts the primary control over wave height transformation across the nearshore in the surf zone across the typical geometry of Type A rock shore platform (1/50 slope), but that dissipation via bottom friction will cause a reduction in wave heights (or less shoaling) seaward of the surf zone. By optimising predicted cross-shore variation in wave height with field observations, the values for the two parameters  $\gamma$  and  $C_f$  can be obtained. In Section 4, shoaling wave data will be used to optimise  $C_f$  for the different field sites, whereas surf zone data will provide the means to optimise  $\gamma$ .

### 3. Methodology



### 3.1. Field sites

Five field deployments were undertaken during the winter months of 2014 – 2015 at four UK and one Irish location with well-developed shore platform morphology (Figure 2), and all representing relatively energetic and large tidal range settings. The sites were Doolin in Ireland (DOL; Figure 2a), Freshwater West in Pembrokeshire, Wales (FWR and FWB, representing both platform and sandy beach sites, respectively; Figure 2b), Lilstock in Somerset, England (LST; Figure 2c), Hartland Quay in north Devon, England (HLQ; Figure 2d), and Portwrinkle in south Cornwall, England (PTW; Figure 2e). These sites, excluding FWR and FWB, have been described by Poate et al. (2016) and site details are summarised in Table 1.

Figure 3 shows the cross-shore profiles of all sites and indicates that a range of platform morphologies are represented in the data. The Doolin platform is relatively narrow ( $x = 160$  m), has the steepest gradient ( $\tan\beta = 0.031$ ) and has a rather stepped morphology due to the limestone beds. The Freshwater West site was chosen to complement the four other deployments as it provided an ideal opportunity to measure two parallel sensor arrays, one across the relatively flat shore platform (FWR;  $\tan\beta = 0.018$ ) and one across the flat sandy beach (FWB;  $\tan\beta = 0.011$ ), to compare bed roughness effects on wave transformation processes under identical forcing. The Lilstock platform experiences the largest tide range (MSR = 10.7 m) and represents the widest platform ( $x = 325$  m), whilst the Hartland Quay and Portwrinkle platforms are both relatively narrow ( $x = 140$  m and  $x = 180$  m, respectively) and steep ( $\tan\beta = 0.030$  and  $\tan\beta = 0.028$ , respectively) platforms. All platforms have some degree of gravel-cobble beach deposit at their landward end, but these are particularly well developed at Hartland Quay and Lilstock. The roughness of the shore platform surfaces will be discussed in Section 4.1, but it can already be observed in Figure 3 that the platforms at Portwrinkle and Lilstock represent the roughest and smoothest surfaces, respectively.

### 3.2. Morphological data

Platform morphology was surveyed using RTK-GPS to obtain representative cross-sections through the instrument arrays (cf. Figure 3). Survey points were taken at least every metre, capturing all significant irregularities and slope breaks. Cross- and alongshore platform variability was mapped at high spatial resolution (3.1 mm at 10 m distance) using a Leica P20 terrestrial laser scanner. A 40-m wide strip of the platform was scanned using 6 – 12 scan positions centred around the instrument array. A digital elevation model (DEM) of the platforms was obtained by interpolating the high-resolution scan onto a regular 0.1 x 0.1 m grid.

The quantification of surface roughness is essential to determine the influence of the platform roughness on wave transformation processes. Two simple measures were used based on 1x1 m square tiles of the platform DEM. The first measure is, analogous to computing the height of wave ripples (Nielsen, 1992), four times the standard deviation associated within the square tiles ( $k_\sigma = 4\sigma_z$ ) and has units of m. Lowe et al. (2005) calculated  $k_\sigma$  using observations of wave dissipation across a coral reef environment, and found typical values of  $k_\sigma = 0.16$  m, which compared very well with measurements of the roughness. The second measure is the rugosity ( $k_R$ ) defined as  $A_r/A_a - 1$  where  $A_r$  is the actual surface area of the square tiles and  $A_a$  is the geometric surface area ( $1 \text{ m}^2$ ). Rugosity is widely used in coral reef studies because it is relatively easy to determine in the field and  $k_R = 0$  (1) for a smooth

(infinitely rough) surface. The estimates of the roughness parameters  $k_\sigma$  and  $k_R$  were alongshore-averaged across the 40-m wide strip to obtain the cross-shore variability in bed roughness.

### 3.3. Hydrodynamic data

Water levels were measured using a shore-normal array of up to fifteen RBR solo D-Wave pressure transducers (PTs), individually housed within steel tubes and fixed to the bedrock with 10 – 15 m spacing. The PTs covered the full spring intertidal zone of the sites to capture shoaling, wave breaking, surf zone and swash conditions, and the deployment strategy was kept consistent to aid comparison between sites. The field deployments lasted 8 – 13 tides with sensors sampling continuously at 8 Hz. Video cameras were used to log the periods of platform inundation during daylight hours. Individual image files were recorded at 4 Hz and used during subsequent processing to identify regions of breaking waves with reference to the pressure sensor locations.

A barometric pressure compensation (determined as the pressure recorded by the (exposed) sensors during each low tide) was used to convert absolute pressure recorded by the PTs to hydrostatic pressure. The dynamic pressure signal was corrected for depth attenuation using a local approximation approach (Nielsen, 1989) and the water depth ( $h$ ) required for this approach was derived using a 10-minute moving average filter.

All data analysis was conducted using 20-min data segments ( $N = 9600$ ); a compromise between limiting tidal non-stationarity in macrotidal settings and having sufficient data length to obtain representative statistical parameters. Spectra were computed using Welch's segment-averaging approach with 8 Hanning-tapered segments overlapped by 50%, providing 16 degrees of freedom. The spectral energy was partitioned into infragravity- and incident-wave energy, with the cut-off frequency separating these two frequency bands determined for each site and for each tide using the high tide wave spectrum from the seaward-most PT. If a spectral valley was present, the frequency associated with the minimum spectral energy was selected as the cut-off; in the absence of a clear spectral valley, a fixed cut-off value of 0.047 Hz was used. No high frequency cut-off was applied. Using the array method of Gaillard et al. (1980), the wave spectra were redefined into incoming and outgoing components, from which the infragravity and incident wave heights ( $H_{s,inf}$  and  $H_{s,inc}$ ) were computed as four times the square root of the total spectral energy summed over the relative frequency bands. The spectral mean wave period was derived from the spectral moments ( $T_{spec} = m_1/m_0$ ). Additional wave parameters computed for the 20-min data segments include the wave power or energy flux ( $P = EC_g$ ) calculated according to linear wave theory (Eqs. (3) and (4)), the wave skewness was calculated from the water surface elevation time series ( $skewness = \sum(n - \bar{n})^3 / \sigma n^{1.5}$ ) where  $n$  = water surface elevation,  $\bar{n}$  = average water surface elevation and  $\sigma$  = variance, while the asymmetry is the skewness of the derivative of the water surface.

To determine the contribution of wave breaking and bed friction to wave energy dissipation, and assess the role of bed roughness in these processes, it is essential to know whether data are from the surf zone or the shoaling wave zone. Additionally, knowledge of the breaker wave height ( $H_b$ ) and breaker depth ( $h_b$ ) are important for normalising the position of the data relative to the breakpoint. For each 20-min data segment, the cross-shore variation in the wave height was used to identify  $H_b$  and  $h_b$  from the maximum wave height in the cross-shore array, with visual calibration performed through the video images whenever possible (Figure 4). If a clear spatial peak in the wave height was not

discernible, usually because the surf zone extended beyond the seaward-most pressure sensor (due to large wave heights and/or low tide level), that data segment was not used for determining the breaker conditions. Then, for every tide, the significant breaker height and the breaker depth were averaged using all data segments for which the breaker conditions could be determined. Due to the very strong tidal currents in the Bristol Channel, the wave conditions at Lilstock exhibit a very pronounced diurnal inequality with the rising tide wave conditions much more energetic than the falling tide conditions; the falling tide data for Lilstock were removed from the analysis.

## 4. Results

### 4.1. Platform roughness

Figure 5 presents the de-trended DEMs of all study sites, including the sandy beach, and the alongshore-averaged bed roughness parameters  $k_\sigma$  and  $k_R$ . The scaling for the DEMs is the same for all sites and it is evident that the surfaces of the shore platforms are highly variable, with Portwrinkle clearly the roughest platform and Lilstock the smoothest. The sandy beach at Freshwater West represents, not surprisingly, by far the smoothest surface. In addition to providing useful insight to the main roughness elements, the DEMs also highlight the geological bedding, which is almost shore-perpendicular at Hartland Quay, oblique to the shore at Freshwater West, almost shore-parallel at Doolin and Lilstock, and complex at Portwrinkle. Faults also contribute to roughness (e.g., Hartland Quay, Portwrinkle).

The visual difference in platform roughness is well quantified by the alongshore-averaged roughness parameters plotted in Figure 5. The roughest platform (Portwrinkle) has typical values for  $k_\sigma$  and  $k_R$  of 0.3 m and 0.2, respectively, the smoothest platform (Lilstock) has values 0.1 m and 0.05, respectively, and the sandy beach 0.01 m and 0.01, respectively. For all sites, the bed roughness parameters do not vary much across the profile and can be characterised by a single value (cross-platform average): variability between the sites is generally greater than variability within the sites. It is noted that the values of the roughness parameters  $k_R$  and especially  $k_\sigma$  increase with the grid size of the DEM. A grid size of 1 m was adopted for all sites; therefore, the roughness values are directly comparable with each other, but not necessarily with that of other studies.

### 4.2. Wave conditions

Considerable variability in the forcing wave conditions was experienced during all field experiments, with offshore significant breaker heights ranging from 0.5 m to 3 m (Figure 6). At all sites, energetic conditions with breaker heights exceeding 1.5 m occurred for multiple tidal cycles, and breaker conditions were generally less energetic than the offshore wave conditions. The largest breaking waves were encountered at Freshwater West ( $H_b = 1.8 - 2.4$  m) and the calmest conditions occurred at Portwrinkle ( $H_b = 0.7 - 1.0$  m).

As detailed in Section 3.3, all data were inspected to identify breaker conditions ( $H_b$  and  $h_b$ ) and tide-averaged  $H_b/h_b$  was found to increase with the breaker wave height. It is not quite clear why this is the case (possibly wave steepness dependency), but because of the large observed variability in  $H_b/h_b$ , with values ranging between 0.25 and 0.6, a tide and site-specific value for  $H_b/h_b$  is used. This value

was used in combination with the local water depth ( $h$ ), to obtain the relative surf zone position ( $h/h_b$ ), where  $h/h_b = 0$  denotes the shoreline and  $h/h_b = 1$  represents the start of the surf zone.

### 4.3. Incident wave height

During all tides and at all sites, the cross-shore variability in the incident wave height measured by the PT array displayed the well-established ‘saturated’ signature in the surf zone with  $H_{s,inc}$  decreasing with decreasing  $h$  (Figure 7). Outside the surf zone,  $H_{s,inc}$  increases up to the breakpoint due to wave shoaling for most data runs. The ratio  $H_{s,inc}/h$  generally increases in the landward direction, both inside and outside the surf zone, in line with predictions according to the Thornton and Guza (1983) model (cf. Figure 1).

The  $H_{s,inc}/h$  values for all data are distributed into class bins and plotted versus the normalised platform/beach slope ( $\tan\beta/kh$ ) and compared to Eq. (1) in Figure 8. Although the trends in the field data are similar to those predicted by Eq. (1), the observed  $H_{s,inc}/h$  values are consistently higher than predicted. This is attributed to differences in the way the raw pressure data were processed: Raubenheimer et al. (1996) removed frequencies  $> 0.18$  Hz from the analysis and did not correct the pressure signal for depth attenuation (an approach that was considered inappropriate for the range of wave periods represented in the current data set and one that would have led to a systematic under-prediction of the data collected under relatively-short period wave conditions). Application of the 0.18-Hz filter by Raubenheimer et al. (1996) is expected to have significantly reduced the incident wave energy and  $H_s$ , and therefore the  $H_{s,inc}/h$  values. The key observation from Figure 8 is that for most sites the  $H_{s,inc}/h$  values are similar with the variability in  $H_{s,inc}/h$  explained reasonably well by the platform/beach gradient and the non-dimensional water depth, parameterised by  $\tan\beta/kh$ . Despite considerable variability in the roughness of the platform surfaces (and sandy beach), it is not apparent that bed roughness plays a significant role in affecting  $H_{s,inc}/h$ . An exception would appear to be at Portwrinkle, which is the roughest platform, where the  $H_{s,inc}/h$  values are smallest and are closest to the predictions by Eq. (1) for the seaward-most data segments (smallest values of  $\tan\beta/kh$ ) and less than the predictions for the landward-most data segments (largest values of  $\tan\beta/kh$ ).

### 4.4. Wave shape

Transformation in wave shape is explored in Figure 9, where wave skewness ( $A_{skew}$ ) and wave asymmetry ( $A_{asym}$ ), computed using the Hilbert transform (cf. Ruessink et al. 2012), are plotted against the normalised surf zone position ( $h/h_b$ ) for each 20-minute data burst. For three of the sites (DOL, FWR, FWB), the skewness increases steadily up to the breakpoint ( $h/h_b = 1$ ) and then decreases towards the shoreline. At HLQ and PTW, the peak in skewness occurs around the mid-surf zone position ( $h/h_b = 0.4 - 0.6$ ), after which  $A_{skew}$  remains constant, whereas at LST, skewness is more or less constant across the entire surf zone. The trends in the wave asymmetry is much more consistent across all sites and  $A_{asym}$  becomes increasingly negative (more asymmetric) towards the shore.

The Ursell number ( $Ur$ ), calculated following Doering and Bowen (1995), gives an indication of the nonlinearity of the waves across the platform at each site, where larger  $Ur$  values represent stronger non-linear effects:

$$Ur = \frac{3}{4} \frac{a_w k}{(kh)^3} \quad \text{Eq. (8)}$$

with  $a_w = 0.5H_s$ . Figure 10 shows the wave skewness and wave asymmetry as a function of the Ursell number. For DOL, FWR and FWB, the skewness values increase from close to zero for low Ursell values ( $Ur < 0.4$ ) and peak at  $A_{skew} = 1 - 1.5$  around  $Ur = 1 - 2$ . For LST, HLQ and PTW there is no clear maximum in skewness and  $A_{skew}$  remains more or less constant at  $A_{skew} = 0.5 - 1$  for  $Ur > 2$ . Wave asymmetry is near-zero for  $Ur < 0.5$  and becomes increasingly negative (increasingly asymmetric in shape) with increasing  $Ur$  values, reaching maximum values near the shoreline ( $A_{asym} < -0.5$ ).

Our results are compared with the predictions of Ruessink et al. (2012):

$$A_{skew} = B \cos\left(\frac{\psi\pi}{180}\right) \quad \text{Eq. (9)}$$

$$A_{asym} = B \sin\left(\frac{\psi\pi}{180}\right) \quad \text{Eq. (10)}$$

where

$$B = P_1 + \frac{P_2 - P_1}{1 + \exp\left(\frac{P_3 - \log Ur}{P_4}\right)} \quad \text{Eq. (11)}$$

$$\psi = 90^\circ + 90^\circ \tanh\left(\frac{P_5}{Ur^{P_6}}\right) \quad \text{Eq. (12)}$$

and  $P_1 = 0$ ,  $P_2 = 0.857 \pm 0.016$ ,  $P_3 = 0.471 \pm 0.025$ ,  $P_4 = 0.297 \pm 0.021$ ,  $P_5 = 0.815 \pm 0.055$ ,  $P_6 = 0.672 \pm 0.073$ , (Figure 10). Skewness at DOL, FWR and FWB is consistently under-predicted, whereas at LST, HLQ and PTW there is a reasonable fit for  $Ur < 2$  but also under-prediction for greater  $Ur$  values. The asymmetry observations at DOL, FWR and FWB match the Ruessink et al. (2012) predictions quite well across the full range of  $Ur$  values, but at LST, HLQ and PTW the  $A_{asym}$  values are under-predicted for  $Ur > 1$ . In summary, in comparison with the predictions of Ruessink et al. (2012), which were derived from data collected on sandy beaches, the waves propagating across the shore platforms appear to have been more skewed at DOL, FWR and FWB indicating enhanced shoaling, and less asymmetric at LST, HLQ and PTW suggestive of not fully-developed asymmetric bores.

#### 4.5. Infragravity wave height

Development of infragravity waves (wave height and percentage energy) across the platforms is expressed against the normalised surf zone position ( $h/h_b$ ) in Figure 11. Incoming infragravity wave heights are greatest at DOL, FWR and FWB ( $H_{s,inf} = 0.5 - 1$  m), while LST and HLQ have the smallest waves ( $H_{s,inf} = 0.1 - 0.3$  m). In the landward direction,  $H_{s,inf}$  increases for DOL, decreases for FWR and FWB, and is relatively constant for the other sites. The decrease at FWR and FWB reflects the dissipation of infragravity energy, observed by De Bakker et al. (2016), where the focus is on incoming infragravity heights not heights as a percentage of the total. At all sites, the proportion of infragravity energy increases in the landward direction. LST stands out as having the smallest proportion of infragravity energy with only a small rise after the breakpoint ( $h/h_b = 1$ ).

Inch et al. (2016), who worked on a low-gradient ( $\tan\beta = 0.015$ ) and high-energy ( $H_s = 1 - 4$  m) dissipative beach, showed that the infragravity wave height could be scaled by an incident wave



power factor  $H_o^2 T_p$  according to  $H_{inf} = 0.004 H_o^2 T_p + 0.2$ , where  $H_{inf}$  is the tidally-averaged total infragravity wave heights ( $H_{inf}$  averaged over each tidal cycle) measured where  $0 < h/h_b < 0.33$ . Recorded values of  $H_{inf}$  are compared with  $H_o^2 T_p$  for each site (**Error! Reference source not found.**) and, with the exception of DOL, the equation proposed by [Inch et al. \(2016\)](#), over-predicts the infragravity wave height for all sites.

#### 4.6. Bulk statistics

For overall comparison between the sites, mid-surf zone position bulk parameters (total wave signals, averaged over all PTs where  $h/h_b = 0.45$  to  $0.55$ ) for  $H_{s,inc}/h$ ,  $A_{skew}$ ,  $A_{asym}$  and  $\%Ig$  are presented in Figure 13 with their corresponding 95 % confidence intervals. Across all of the parameters and sites, there are a number of statistically significant differences (indicated by non-overlapping CI's), but few clear trends exist for any one location and there are no sites that consistently score highest/lowest. In terms of similarity, the data can be grouped as follows: (1) DOL and FWR have the highest  $H_{s,inc}/h$  and  $\%Ig$  values and are the most non-linear (both in terms of skewness and asymmetry; (2) LST, HLQ and PTW are characterised by the lowest  $H_{s,inc}/h$  and  $\%Ig$  values, and are the least non-linear; and (3) FWB falls very much between these two groups in all aspects, except for  $H_{s,inc}/h$ , where it is characterised by the lowest value, although this could be due to a limited number of measurements from the inner-surf zone region. The link between the bulk parameters and platform roughness will be addressed within the discussion.

A strong association appears to be present between the proportion of infragravity energy ( $\%Ig$ ) and the wave asymmetry ( $A_{asym}$ ). DOL and FWR have the largest  $\%Ig$  compared to the other sites and are characterised by the most asymmetric (pitched-forward) wave form; the sites with the least asymmetric surf zone waves (LST, HLQ and PTW) were characterised by the lowest  $\%Ig$  values. Greater values of  $A_{asym}$  suggests enhanced bore development and more intense short-wave dissipation.

#### 5. Numerical Model

The purpose of the energy flux model (**Eq. 2**) is to support the field observations by exploring the parameter space of  $\gamma$  and  $C_f$  relative to platform roughness. The model is initialised at the seaward boundary ( $x = 0$  m) using observations from the most offshore PT. A normalised cross-shore grid spacing of  $\Delta x' = \Delta x / T_p \sqrt{g H_o} = 0.01$ , where  $\Delta x$  is the dimensional grid size, is used and the profile smoothed with a 6-m moving-average filter (determined using a convergence test) to minimise small-scale steps in the bathymetry caused by the geometry of individual rock elements. First, the model is calibrated for the free parameters  $\gamma$  and  $C_f$  which control the dissipation by wave breaking and friction, respectively.

Seaward of the surf zone, the dissipation of short wave energy is dominated by bottom friction and is therefore principally controlled by the bed roughness; this zone can therefore be used to calibrate  $C_f$ . Data from four tides from each field site (excluding FWB where the PT array was too short to permit reliable model optimisation) were used to calibrate the model, totalling approximately 750 model simulations. To calibrate  $C_f$ , we only used data recorded from seaward of the surf zone. A strict a-priori assumption of the breaker criterion  $\gamma$  ( $H_{s,inc}/h$ ) for the region seaward of the surf zone was determined by a visual inspection of the data bursts from each tide (typically  $H_{s,inc}/h = 0.28 - 0.42$ ) as described in Section 3.3, identifying those PTs which were very clearly located seaward of the surf zone and where dissipation must be solely due to bottom friction. The model was run for each of these

tides over a range of  $C_f$  and with  $\gamma$  set to 0.42, a typical value from the existing literature (e.g., Thornton and Guza, 1983). The optimum value for  $C_f$  was determined by minimising error estimates between the observed and modelled wave heights across the region seaward of the surf zone.

To quantify the model error, the absolute root-mean-square error  $\epsilon_{abs}$  and relative bias  $\epsilon_{bias}$  were computed by comparing the incident wave height  $H_{s,inc}$  obtained from the measurements ( $M$ ) with the computed  $H_s$  ( $C$ ) at each PT location ( $i$ ) and for each 10-minute burst ( $t$ ), and where  $|-|$  indicates the modulus and  $\langle - \rangle$  the mean, respectively:

$$\epsilon_{abs} = \sqrt{\langle C_{(i,t)} - M_{(i,t)} \rangle^2} \quad \text{Eq. (13)}$$

$$\epsilon_{bias} = \sqrt{\langle C_{(i,t)} - M_{(i,t)} \rangle^2} / \max_{0 \rightarrow \infty}(\epsilon_{abs}, |\langle M_{(i,t)} \rangle|) \quad \text{Eq. (14)}$$

Values of  $\epsilon_{abs}$  and  $\epsilon_{bias}$  tending to zero indicate higher model performance. The most offshore PT was excluded from the calibration, since data from this location are used as the seaward boundary forcing for the model, and are thus not independent. This calibration was repeated for all field sites and the optimum  $C_f$  for each site was determined by minimising the rms and bias errors for every burst within each tide and computing the mean  $C_f$  by averaging the rms and bias errors (Figure 14). DOL, HLQ and PTW display parabolic curves of the distribution of the rms error for  $C_f$ , with the optimum  $C_f$  indicated by the minima. However, for FWR and LST the error curves asymptotically tend towards zero, indicating an effective model  $C_f$  of zero. The distribution of the bias displays a similar pattern across the field sites, and indicates that the shoaling wave heights at FWR and LST are under-predicted, which explains why the optimisation is driving  $C_f$  towards zero at these sites.

Inside the surf zone, however, wave energy is dissipated by both bottom friction and wave breaking. The model was calibrated for  $\gamma$  by optimising model performance for PTs determined to be within the surf zone, with  $C_f$  set to the value determined above for the region seawards of the surf zone. As for  $C_f$  above, the optimum  $\gamma$  for each field site was determined as the mean  $\gamma$  of the combined rms and bias errors for each tide (Figure 15). The results for the calibration of  $\gamma$  display clear parabolic curves for the rms errors at all sites except PTW, which tends to increase towards larger values of  $\gamma$ , and the results are consistent between rms and bias errors.

Example model outputs for each platform are compared to field observations in Figure 16. Absolute root mean square errors for  $H_s$  are  $O(10^{-2})$ m based on the four calibration tides at all platforms, and qualitatively the model performance is very good at all cross-shore locations, except at the very shallow landward-most PT at DOL and FWR, which experience significant wave reflection, wave set-up and non-linear processes not included in the simple model, and the mid-surf zone region at PTW. Rates of wave energy dissipation are also well predicted and reveal that frictional dissipation appears to be negligible at all sites except PTW. At PTW, frictional dissipation is observed to increase moving landwards from the shoaling wave to surf zone, presumably as wave orbital velocities increase under the breaking waves, but breaker dissipation remains the dominant in the surf zone. It is noteworthy that there are several large spikes of predicted dissipation (i.e., at DOL and PTW) that are not observed in the field observations. These result from instantaneous model dissipation over step changes in profile bathymetry to which the waves observed in the field do not appear to immediately respond and it results in the overall model error being greatest for PTW. A landward increase in  $H_{s,inc}/h$  (typically 0.4 – 1.0) is observed for both the field and model data. This is consistent with the observations of Ogawa et al. (2011) and is the expected model behaviour when wave breaking is the

dominant mode of dissipation (Figure 1). It is well predicted by the model at all sites except HLQ, which displays a consistent over-prediction at the landward end of the platform; it is unclear why this is the case.

The dissipation parameters determined via the optimisation of the energy flux model, averaged over the four tides at each field site, are presented in Table 2. The combined estimates of  $\gamma$  and  $C_f$  from the model provide an indication of the relative importance of short-wave dissipation by bottom friction and by wave breaking over the rock platforms. The optimised  $\gamma_s$  range from 0.51 at DOL to 0.93 at PTW, which extends from the upper range typically reported from sandy beaches ( $\sim 0.5 - 0.64$ ) to significantly higher values. The optimised  $C_f$  are highly variable, ranging from  $O(10^{-4})$  at FWR and LST to  $O(10^{-1})$  at PTW. Qualitatively, the  $C_f$  values for LST (smoothest) and PTW (roughest) are consistent with the observed platform roughness length-scales  $k_\sigma$  and  $k_R$ , but it is unclear why it is so low for FWR, the second roughest site. The mean ratio of frictional to breaker dissipation  $\langle \varepsilon_f / \varepsilon_b \rangle$  at the mid-surf zone position ( $0.45 \geq h/h_b \geq 0.55$ ) for all tides examined is typically  $< 0.15$  (Table 2); only at PTW does friction dominate where  $\langle \varepsilon_f / \varepsilon_b \rangle = 3.82$ .

## 6. Discussion

### 6.1 Analysis of field data

Field data collected from five sloping (Type A) rock shore platforms (Sunamura, 1992) and one intertidal beach were used to study wave transformation processes across the intertidal surfaces and specifically address the role of surface roughness on wave transformation. Due to the different lithology and bedding types, the five shore platforms represent a range in surface gradient and roughness. The platforms at Freshwater West (FWR) and Lilstock (LST) are relatively gently-sloping ( $\tan\beta = 0.018$  and  $0.021$ , respectively) and the steeper platforms are present at Portwrinkle (PTW), Hartland Quay (HLQ), and Doolin (DOL) ( $\tan\beta = 0.028, 0.30$ , and  $0.31$ , respectively). LST represents the smoothest surface ( $k_R = 0.015$ ) and the roughest platform is at PTW ( $k_R = 0.090$ ). The beach site FRB is characterised by the gentlest gradient ( $\tan\beta = 0.011$ ) and the smoothest surface ( $k_R = 0.002$ ). During the fieldwork the different sites experienced varying wave and tidal conditions, with PTW and FWR representing the smallest and largest waves ( $H_b = 0.7 - 1.0$  m and  $H_b = 1.7 - 2.5$  m, respectively), and DOL and LST experiencing the smallest and largest tides ( $MSR = 4.2$  m and  $MSR = 10.7$  m, respectively). A large number of pressure sensors (12 – 15) were deployed in a single transect across each shore platform and data were collected over 8 – 13 tides. This dataset represents the most extensive ever collected on rocky shore platforms, both in terms of the range of environmental conditions experienced, and the duration and spatial resolution of the measurements. It also represents the only wave transformation data set so far collected on Type A platforms, as all previous studies have been conducted on sub-horizontal Type B platforms.

In agreement with all previous studies of wave transformation across shore platforms, wave energy is strongly tidally-modulated and is depth-limited (i.e., saturated) across the inner part of the intertidal region (e.g., Farrell et al., 2009; Marshall and Stephenson, 2011; Ogawa et al., 2011). Additionally, the relative contribution of infragravity energy to the total wave energy content in the surf zone increases in a landward direction (cf., Beetham and Kench, 2011; Ogawa et al., 2015). We also demonstrate that the absolute infragravity energy level, quantified by the incoming infragravity wave height, decreases in the landward direction. The intertidal shore platforms, therefore, represent effective dissipaters of both incident and infragravity energy. As the waves propagate and dissipate across the platform, there are also systematic changes in the wave shape: wave skewness increases up



to the seaward extend of the surf zone and then decreases (DOL, FWR, FWB) or stays more or less constant (HLQ, LST, PTW), and at all sites the wave asymmetry becomes increasingly negative in the landward direction indicating the presence of turbulent and forward-pitching bores, indicative of continuous wave breaking.

The local wave height to water depth ratios  $H_{s,inc}/h$  calculated here over the shore platforms compare favourably with those reported where wave breaking is the dominant form of dissipation over sandy beaches (Raubenheimer et al., 1996), near-horizontal rock platforms (Ogawa et al., 2011) and the fore reef of coral reefs (Vetter et al., 2010). Significantly, the consistent landwards increase in  $H_{s,inc}/h$  indicates that dissipation by wave breaking is a continuous process across the platforms, confirmed by the observed landward increase in negative wave asymmetry, and that at any cross-shore location there is a combination of breaking and broken waves. This contrasts to observations across similarly rough (or rougher) coral reefs platforms, where the initial peak in  $H_{s,inc}/h$  observed as waves break on the steep fore reef is followed by a decrease in  $H_{s,inc}/h$  as energy dissipation becomes dominated by frictional drag with no breaking over the sub-horizontal reef flat (Lowe et al., 2005; Vetter et al., 2010, Rodgers et al., 2016). This difference occurs because the shore platforms studied here have relatively steep and near-constant planar slopes, whereas on coral reefs there is a clear distinction between the steeply-sloping fore reef and the sub-horizontal reef platform. As such, the morphology of coral reefs is rather similar to that of Type B shore platforms; therefore, care should be taken in extrapolating the present findings derived from Type A platforms to Type B platforms.

The aim of this paper is to investigate whether wave transformation processes on shore platforms are different from that on sandy beaches due to differences in bed roughness. The approach has been to compare observed data trends in terms of relative wave height ( $H_{s,inc}/h$ ), wave skewness ( $A_{skew}$ ), wave asymmetry ( $A_{asym}$ ) and incoming infragravity wave height ( $H_{s,inf}$ ) between the different platforms and with expressions related to these parameters from the literature derived from sandy beaches. The systematic landwards increase in  $H_{s,inc}/h$  was linked to the normalised slope  $\tan\beta/kh$  using **Eq. 1** based on Raubenheimer et al. (1996), which combines the non-dimensional water depth  $kh$  with the bed gradient  $\tan\beta$ , and which provides a good description of the data (accounting for under-prediction due to the difference in data filtering prior to analysis; cf., Section 4.3). The dependence of  $H_{s,inc}/h$  on  $\tan\beta$  is also evident when comparing across the different platform sites, with the steeper platforms DOL, HLQ, PTW displaying larger surf zone values of  $H_s/h$  than the flatter platforms LST and FWR and particularly the beach FWB. This is consistent with studies on sandy beaches (e.g., Sallenger and Holman, 1985; Masselink and Hegge, 1996). No obvious control of the platform roughness on  $H_{s,inc}/h$  could be discerned. The development of wave non-linearity (skewness and asymmetry) was compared with formulations (**Eqs. 9 – 12**) suggested by Ruessink et al. (2012). The qualitative trends in the data, as a function of the Ursell Number ( $Ur$ ; **Eq. 8**), are well represented by these equations, specifically the increase then decrease in wave skewness, which peaks at  $Ur = 1 - 2$ , and the progressive increase in negative wave asymmetry with decreasing  $Ur$ . The most pitched-forward surf zone waves (most negative  $A_{asym}$ ) and the highest skewness values were observed at the sites which experienced the most energetic wave conditions (DOL, FWR, FWB), and no obvious influence of platform roughness on wave shape was observed. When compared with sandy beaches, the spatial trends in wave shape is similar, which would suggest the role of roughness is not significant.

Following the work of Inch et al. (2016), the total infragravity wave height ( $H_{inf}$ ), where  $0 < h/h_b < 0.33$ , was related to a wave power parameter ( $H_o^2 T_p$ ). With the exception of DOL for some tides, the observed values of  $H_{inf}$  are consistently over-predicted by the formulation of Inch et al. (2016). We attribute this to enhanced friction imparted on the infragravity wave motion by the rough platform

surfaces, leading to suppressed infragravity wave energy in the (inner) surf zone. This suggestion is supported by [McCall et al. \(2017\)](#) who used the current data set and the XBeach numerical model to investigate the relationship between the drag coefficient (used for parameterising friction for steady currents and infragravity wave motion) and the platform roughness. They found that if a smoothed rock platform profile was used, the drag coefficient required to provide the best agreement between observed and modelled infragravity wave energy levels increased with platform roughness.

In a final attempt to identify a demonstrable influence of platform roughness on wave transformation parameters, average values for a range of variables were computed for each of the platforms. The ‘independent’ variables selected are wave power ( $H_b^2 T$ ; averaged over all tides with data), platform gradient ( $\tan\beta$ ) and platform roughness ( $k_\sigma$  and  $k_R$ ), and are listed in Table 1. The ‘dependent’ variables are relative wave height ( $H_{s,inc}/h$ ), percentage incoming infragravity wave height ( $\%H_{s,inf}$ ), wave skewness ( $A_{skew}$ ) and wave asymmetry ( $A_{asym}$ ). The dependent variables were averaged for each of the sites, but only for data from the mid-surf zone position ( $h/h_b = 0.45 - 0.55$ ), and are shown in Figure 13. A correlation matrix was constructed (not shown), and only four correlations were statistically significant at a level higher than 0.1. Strong correlations were obtained between the different wave parameters: wave skewness was correlated with the breaking wave power ( $r = 0.88$ ;  $p = 0.02$ ), whereas wave asymmetry was correlated with the percentage of incoming infragravity energy ( $r = -0.85$ ;  $p = 0.03$ ). Finally, a weak correlation was found between the bed gradient and the relative wave height ( $r = 0.72$ ;  $p = 0.10$ ), supporting previous work on sandy beaches (e.g., [Raubenheimer et al., 1996](#)). Most importantly, none of the dependent variables are correlated to the platform roughness.

## 6.2 Numerical modelling

The simple numerical model of [Thornton and Guza \(1983\)](#) was used to support the field observations and investigate the dissipation of the incident wave energy across the platforms by wave breaking and bottom friction, parameterised by  $\gamma_s$  and  $C_f$ , respectively. The optimised values for the model breaker criteria  $\gamma_s$  (0.51 – 0.93, Table 2) are larger than the observed bulk mid-surf zone values of  $H_{s,inc}/h$  (Figure 13a) for all sites except DOL, but encouragingly fall between the range of values reported in the literature for sandy beaches (0.4 – 0.59) ([Thornton and Guza, 1983](#); [Sallenger and Holman, 1985](#); [Raubenheimer et al., 1996](#)) and coral reefs (0.59 – 1.15) ([Lowe et al., 2005](#); [Vetter et al., 2010](#); [Péquignat et al., 2011](#)). The result of the calibration for  $C_f$  is less clear, since, although the optimum value of  $C_f$  at LST (0.005), DOL (0.05), HLQ (0.049) and PTW (0.34) reflect the increasing hydraulic roughness of these platforms, the range of  $C_f$  spans two orders of magnitude.  $C_f$  was also estimated from the data for the tides used in the model calibration by regressing the measured rate of dissipation **Eq. (2)** across all adjacent PT pairs in the region seaward of the breakers against **Eq. (6)**, where  $C_f$  is the regression coefficient (e.g., [Wright et al., 1982](#)). A large amount of scatter was observed in the data that was attributed to strongly shoaling waves, but statistically significant ( $p < 0.05$ ) estimates of  $C_f \approx 0.1$  were obtained for DOL, LST and PTW, which fall within the range of values obtained from the model calibration. Whilst this large range leads us to question how representative the calibrated values of  $C_f$  are, it is encouraging that except for LST (where  $C_f$  is very small), the values fall within the region between sandy beaches (0.01, e.g., [Thornton and Guza, 1983](#)) and coral reefs (0.16, 0.22 and 1.8, [Lowe et al., 2005](#); [Falter et al., 2004](#); [Monismith et al., 2015](#)); therefore, we also compare our calibrated values of  $C_f$  with the empirical wave friction model of [Nielsen \(1992\)](#) to gain further insight.

[Nielsen \(1992\)](#) predicts the wave friction factor  $f_w$  for rough turbulent boundary layers as a function of the ratio of the near-bed horizontal wave orbital amplitude  $A_b$  to the hydraulic roughness length-scale  $k_w$  (e.g., [Jonsson, 1966](#); [Swart, 1974](#); [Madsen, 1994](#))

$$f_w = \exp \left[ 5.5 \left( \frac{A_b}{k_w} \right)^{-0.2} - 6.3 \right]. \quad \text{Eq. (17)}$$

The value of  $k_w$  is usually specified as a function of the grain diameter  $D$ , where  $k_w = 2D$  (Nielsen, 1992). To be consistent with the definition in Eq. (17),  $D \approx 2\sigma_r$ , where  $\sigma_r$  is the roughness amplitude and  $k_w = 4\sigma_r$  (e.g., Lowe et al., 2005). Applying Eq. (17) to the roughness estimated using the terrestrial laser scanner,  $k_w \equiv k_\sigma$  (Figure 5; Table 1), allows a comparison with the predicted drag coefficient  $C_f$  derived from the numerical model through the relationship  $f_w = 2C_f$ . The mean drag coefficients computed over the four model optimisation tides for all of the platforms using Eq. (17) are  $O(10^{-2})$  with the smallest value associated with the smoothest platform (LST, 0.0225) and the largest with the roughest (PTW, 0.069). Comparing these empirical estimates with those determined via the numerical model optimisation shows that the trends in  $C_f$  are well replicated when FWR is excluded, and that for our middle range of platforms DOL and HLQ ( $\tan\beta \sim 0.03$ ,  $k_\sigma \sim 0.02$ ), the empirical and numerical estimates are in close agreement. For the roughest platform PTW,  $C_f$  is under-predicted, but Nielsen (1992) notes that  $f_w$  and  $C_f$  are very similar for friction coefficients  $>0.05$ , so by ignoring the phase lag between the flow velocity and bed shear stress we could assume that  $f_w = C_f$  at PTW, which would increase the empirically-derived  $C_f$  towards that derived from the model calibration.

After optimisation of the numerical model, typical rms errors between predicted and observed  $H_s$  are consistently small (3 – 10 cm) and the distribution of wave energy dissipation is generally well replicated (Figure 16). The model results indicate that breaking wave dissipation dominates across all platforms except PTW and, in line with the field observations, do not show any systematic variations in the wave height decay between sites that can be linked to platform roughness. The predicted  $H_{s,inc}/h$  compare well with the observations at the majority of the platform sites, in particular DOL, LST and PTW, which all display the strong landwards increase in  $H_{s,inc}/h$  associated with the increasing proportion of broken wave bores towards the shoreline. This suggests that the Rayleigh distribution inherent in the model formulation (Eq. 5 and Figure 1) can be used to successfully parameterise the wave height dissipation by wave breaking across the majority of the rock platforms studied.

The results of the numerical model generally agree well with the field observations (i.e., Figure 16) and the range of computed  $H_{s,inc}/h$  fall within the expected range between sandy beaches and coral reefs; however, there are concerns about the calibration of  $C_f$  that question the suitability of the model. This is highlighted by the very high optimised  $C_f$  for PTW (0.34), the roughest platform, and the very low optimised  $C_f$  for FWR (0.005), also a very rough site. In the present study, both  $C_f$  and  $\gamma$  are independently calibrated, while in studies of wave propagation over reefs it is common to fix one of the dissipation parameters and calibrate for the other (e.g., Lowe et al., 2005; Péquignot et al., 2011). When the optimised  $C_f$  is replaced by Nielsen's (1992) empirical estimate (or the data-derived values) and the model is recalibrated for  $\gamma$ , larger rms errors for  $H_{s,inc}$  are obtained (not shown). Certainly, for the roughest platforms PTW and FWR, the ratio  $A_b/k_w$  in Eq. (17) for the incident-wave frequencies approaches unity, which means that the wave orbital length-scale is similar to the roughness length scale (Madsen, 1994). This may imply that the numerical model used here incorrectly parameterises the physics of wave-roughness interaction across a very rough rock platform, and suggests an alternative parameterisation may be required. One approach could be to specify a relative roughness linked to the large-scale morphology of individual platform roughness elements. These are often of a similar height or diameter to the surf zone water depth and directly affect the passage of waves, which must flow around and over such structures. A parameterisation similar to that of flow through canopies, where  $f_w \propto \alpha_w$ , may be more appropriate, where  $\alpha_w$  is the ratio of the flow in the canopy to

that just above the canopy, which is shown to depend on the ratio of the spacing of the canopy elements to  $A_b$  (e.g., [Lowe et al., 2007](#); [Huang et al., 2012](#); [Monismith et al., 2015](#)). Therefore, for very rough rock platforms, frictional drag may scale with the ratio of the rock element spacing to  $A_b$ ; however, this requires further investigation by field observation and higher-order numerical modelling, since [Rodgers et al. \(2016\)](#) do correlate  $f_w$  to  $A_b/k_w$  across an exceptionally rough coral reef.

### 6.3 Implications for wave dissipation over rock platforms

Under the conditions during which we collected our data, there does not appear to be a significant impact of roughness on wave energy dissipation; however, there may be conditions when bed friction becomes important (e.g., [Lowe et al., 2005](#)). Whilst we have some concerns about the applicability of several of the model results, there is sufficient confidence, inspired by the good fit in Figure 16 and the skilful quantification of  $H_{s,inc}/h$  across our middle range of sites, to use the model to investigate the importance of frictional dissipation across a shore platform.

Wave energy dissipation by bed friction  $\varepsilon_f$  was integrated across the intertidal region of a Type A shore platform for varying wave conditions, bed gradients and  $C_f$  values. Two of these parameters were fixed at the mean observed values and a number of simulations were run by varying the remaining input parameters (Figure 17). The relative importance of frictional dissipation increases with decreasing wave height and bed gradient, and increasing bed roughness. The absolute values for the wave dissipation by friction increase with increasing wave height and bed roughness, and decreasing bed gradient. These results indicate that frictional dissipation is only significant on platforms that are very rough ( $C_f > 0.1$ ), low-gradient ( $\tan\beta < 0.02$ ) and/or subjected to small wave conditions ( $H_o < 0.5$  m), where friction may account for ~20 % of the total wave energy dissipation. However, under small waves, the absolute amount of energy dissipated is very small ( $< 1$  kW m<sup>-2</sup>), so across these very rough flat platforms the total amount of frictional dissipation scales with  $H_o$ . This implies that over the majority of Type A rock shore platforms short-wave breaking is the dominant source of dissipation and the effects of bottom friction are small ( $< 10$  % of the total), so can probably be disregarded in wave energy balance models. Further analysis using models with more physical processes (e.g., phase-resolving, or surf-beat models) is required to similarly investigate the sensitivity of nearshore currents and infragravity waves to the bed roughness of the platforms.

Finally, we briefly revisit the morphological implications of our findings to discuss the role of wave action in the evolution of rocky coasts. Type A shore platforms primarily dissipate energy by wave breaking, which drives mean near-bed currents through the generation of radiation stress gradients ([Longuet-Higgins and Stewart, 1962](#)). These currents will impart a drag force onto the rock surface, acting to cause direct platform erosion (e.g., through hydraulic plucking of weathered, fractured rock), and abrasion by the transport of loose materials across its surface ([Sunamura, 1992](#)). Wave dissipation by bed friction is of secondary importance and it is only important where the turbulence associated with the broken waves reaches the bed at the shallow landward extreme of the platform that wave forces have a direct effect on platform erosion. This conjures up an image of a wide turbulent surf zone, effective at dissipating wave energy, but only able to leverage this energy for doing geomorphological work within a narrow shallow-water region. This narrow turbulent region, comprising of the swash and inner surf zone, migrates twice-daily across the platform due to the tide, and it is in this zone where most of the geomorphic work is considered being done. Considering platforms such as DOL with slab-like steps in the upper-profile, we may expect slabs to be loosened by direct wave forcing and then removed by the mean wave-generated near-bed currents ([Stephenson and Naylor, 2011](#)). Conversely, at HLQ wave-generated currents are probably focused into the channels formed by the cross-shore orientation of the bedding planes, directly eroding rock fragments



and causing abrasion. Lastly, it appears to be the gradient of the Type A platform that determines the delivery of wave energy, and hence potential for cliff toe erosion (Naylor et al., 2010), by controlling the cross-shore distribution of the rate of wave breaking dissipation. We thereby suggest that for the purposes of determining the role of waves in cliff erosion and rocky shore evolution, the majority of Type A shore platforms may be modelled in a similar manner to a sandy beach.

## 7. Conclusions

Here we present for the first time a comprehensive analysis of wave transformation across sloping (Type A) rock shore platforms. Observations from five platforms, all with contrasting surface roughness, gradient and wave climate, represent the most extensive ever collected on rock shore platforms and demonstrate that frictional dissipation by platform roughness is of secondary importance compared to wave breaking dissipation. This is similar to observations on smooth sandy beaches, but is in contrast to rough coral reef platforms where friction has been observed to dominate. Rock platforms are shown to dissipate both incident and infragravity wave energy and, in line with previous studies, surf zone wave heights are saturated and strongly tidally-modulated. Waves develop skewness and asymmetry across the platforms, and the relative wave height to water depth ratio scales with platform gradient. Overall, comparisons between the observed properties of the waves and formulations derived from sandy beaches has not highlighted any systematic variations between the sites that can be attributed to (differences in) platform roughness.

Optimisation of a simple numerical wave transformation model provides further exploration of the frictional and wave breaking parameter space. The breaker criterion falls between the range of values reported for flat sandy beaches and steep coral fore-reefs, lending further support to the control by platform gradient; however, the optimised drag coefficient for frictional wave dissipation is significantly scattered for the roughest sites. Further exploration using an empirical drag coefficient does not improve performance and suggests that high-order numerical wave models are required to successfully parameterise frictional dissipation over the roughest platforms.. Model simulations using a range of average data from our most typical platforms indicate that friction accounts for ~10 % of the total intertidal short-wave dissipation under modal wave conditions, only becoming significant (~20 %) across very rough, flat platforms, under small wave conditions. Overall, observational and modelling results suggest that frictional dissipation of short-wave energy can probably be neglected for the majority of Type A rock platforms, particularly inside the surf zone, which can be treated similarly to sandy beaches when assessing wave energy delivery to the landward end of the platforms.

## Acknowledgements

This research was funded by EPSRC grant EP/L02523X/1, Waves Across Shore Platforms, awarded to GM and MJA. We would like to thank our field and technical team: Peter Ganderton, Tim Scott, Olivier Burvingt, Pedro Almeida, Kris Inch and Kate Adams. The data on which this paper is based is available from TP or via the online repository found at <http://hdl.handle.net/10026.1/9105>. The authors would like to thank the reviewers who provided valuable feedback, insight and comment on the original manuscript and, we believe, improved the work as a result.

## 8. References;

- Battjes, J.A., and J.P. Janssen (1978). Energy loss and setup due to breaking of random waves. Proc. 16th ICCE, ASCE, 569-588, doi 10.1061/9780872621909.034.
- Beetham, E., and P.S. Kench (2011). Field observations of infragravity waves and their behaviour on rock shore platforms. ESPL, doi: 10.1002/esp.2208.

- Brander, R. W., P. S. Kench, and D. Hart (2004), Spatial and temporal variations in wave characteristics across a reef platform, Warraber Island, Torres Strait, Australia, *Marine Geology*, 207(1–4), 169–184. Doi: 10.1016/j.margeo.2004.03.014.
- De Bakker, A.T.M., Brinkkemper, J.A., Van der Steen, Florian, Tissier, M.F.S. & Ruessink, B.G. (2016). Cross-shore sand transport by infragravity waves as a function of beach steepness. *Journal of geophysical research. Earth surface*, 121 (14 p.).
- Dickson, M. E., M. J. A. Walkden, and J. W. Hall (2007), Systemic impacts of climate change on an eroding coastal region over the twenty-first century, *Climatic Change*, 84(2), 141–166. Doi: 10.1007/s10584-006-9200-9.
- Dickson, M. E., and R. Pentney (2012), Micro-seismic measurements of cliff motion under wave impact and implications for the development of near-horizontal shore platforms, *Geomorphology*, 151–152, 27–38. Doi: 10.1016/j.geomorph.2012.01.006.
- Dickson, M. E., H. Ogawa, P. S. Kench, and A. Hutchinson (2013), Sea-cliff retreat and shore platform widening: steady-state equilibrium?, *Earth surface processes and landforms*, 38(9), 1046–1048. Doi: 10.1002/esp.3422.
- Doering, J. C., and A. J. Bowen (1995), Parametrization of orbital velocity asymmetries of shoaling and breaking waves using bispectral analysis, *Coastal Engineering*, 26(1-2), 15–33. Doi: 10.1016/0378-3839(95)00007-X.
- Farrell, E. J., H. Granja, L. Cappiotti, J. T. Ellis, B. Li, and D. J. Sherman (2009), Wave Transformation across a Rock Platform, Belinho, Portugal, *Journal of Coastal Research*, 44–48.
- Falter, J. L., M. J. Atkinson, M. A. Merrifield (2004), Mass-transfer of nutrient uptake by a wave-dominated reef flat community, *Limnology and Oceanography*, 49(5), 1820–1831.
- Hardy, T. A., and I. R. Young (1996), Field study of wave attenuation on an offshore coral reef, *Journal of Geophysical Research: Oceans*, 101(C6), 14311–14326. Doi: 10.1029/96JC00202
- Huang, Z.-C., L. Lenain, W. K. Melville, J. H. Middleton, B. Reineman, N. Statom, and R. M. McCabe (2012), Dissipation of wave energy and turbulence in a shallow coral reef lagoon, *Journal of Geophysical Research: Oceans*, 117(C3). Doi: 10.1029/2011JC007202
- Inch, K., Davidson, M., Masselink, G. and Russell, P., (2017), Observations of nearshore infragravity wave dynamics under high energy swell and wind-wave conditions. *Continental Shelf Research*, 138, 19–31.
- Kench, P. S., R. W. Brander, K. E. Parnell, and R. F. McLean (2006), Wave energy gradients across a Maldivian atoll: Implications for island geomorphology, *Geomorphology*, 81(1–2), 1–17.
- Kennedy, D. M., and J. Milkins (2015), The formation of beaches on shore platforms in microtidal environments, *Earth surface processes and landforms*, 40(1), 34–46. Doi: 10.1002/esp.3610
- Kennedy, D. M., R. Paulik, and M. E. Dickson (2011), Subaerial weathering versus wave processes in shore platform development: reappraising the Old Hat Island evidence, *Earth surface processes and landforms*, 36(5), 686–694. Doi: 10.1002/esp.2092
- Kobayashi, N., and A. Wurjanto (1992), Irregular Wave Setup and Run-up on Beaches, *Journal of Waterway, Port, Coastal, and Ocean Engineering*, 118(4), 368–386. Doi: 10.1061/(ASCE)0733-950X(1992)118:4(368)

- Komar, P.D., 1998. Beach Processes and Sedimentation. Prentice-Hall, Upper Saddle River, NJ, 544 pp.
- Lowe, R. J., J. L. Falter, M. D. Bandet, G. Pawlak, M. J. Atkinson, S. G. Monismith, and J. R. Koseff (2005), Spectral wave dissipation over a barrier reef, *Journal of Geophysical Research: Oceans*, 110(C4). Doi: 10.1029/2004JC002711.
- Lowe, R. J., J. L. Falter, J. R. Koseff, S. G. Monismith, and M. J. Atkinson (2007), Spectral wave flow attenuation within submerged canopies: Implications for wave energy dissipation, *Journal of Geophysical Research: Oceans*, 112(C5), 1 – 14. Doi: 10.1029/2006JC003605
- Madsen, O. S., 1994. Spectral wave-current bottom boundary layer flows, in Coastal Engineering 1994: Proceedings of the Twenty-Fourth International Conference, edited by B. L. Edge, pp. 623 – 634, Am. Soc. of Civ. Eng., Reston, Va.
- Marshall, R. J. E., and W. J. Stephenson (2011), The morphodynamics of shore platforms in a micro-tidal setting: Interactions between waves and morphology, *Marine Geology*, 288(1–4), 18-31. Doi: 10.1016/j.margeo.2011.06.007
- May, V.J. and Hansom, J.D., (2003). Coastal Geomorphology of Great Britain, Geological Conservation Review Series, No. 28, Joint Nature Conservation Committee, Peterborough, 754 pp.
- Masselink, G. and Hegge, B., (1995). Morphodynamics of meso- and macrotidal beaches: examples from central Queensland, Australia. *Marine Geology*, 129(1-2): 1-23. Doi: 10.1016/0025-3227(95)00104-2
- McCall, R., Masselink, G., Austin, M., Poate, T. and Jager, T., (2017) Modelling Incident-Band and infragravity wave dynamics on rocky shore platforms. Proceedings of Coastal Dynamics 2017, Denmark. Pp1658-1669.
- Monismith, S. G., J. S. Rogers, D. Kowek, and R. B. Dunbar (2015), Frictional wave dissipation on a remarkably rough reef, *Geophysical Research Letters*, 42(10), 4063-4071. Doi: 10.1002/2015GL063804.
- Naylor, L. A., W. J. Stephenson, and A. S. Trenhaile (2010), Rock coast geomorphology: Recent advances and future research directions, *Geomorphology*, 114(1–2), 3-11. Doi: 10.1016/j.geomorph.2009.02.004.
- Nielsen, P., (1992). Coastal bottom boundary layers and sediment transport. Advanced Series on Ocean Eng. vol. 4. World Scientific, Singapore, pp. 324.
- Nielsen, P., (1989). Analysis of Natural Waves by Local Approximations. *Journal of Waterway, Port, Coastal, and Ocean Engineering*, 115(3): 384-396. Doi: 10.1061/(ASCE)0733-950X(1989)115:3(384).
- Nelson RC. (1994). Depth limited design wave heights in very flat regions. *Coastal Engineering* 23(1 – 2): 43 – 59. Doi: 10.1016/0378-3839(94)90014-0.
- Nott, J. (2003), Waves, coastal boulder deposits and the importance of the pre-transport setting, *Earth and Planetary Science Letters*, 210(1–2), 269-276. Doi: 10.1016/S0012-821X(03)00104-3.

- Ogawa, H., Dickson, M. E., & Kench, P. S. (2015). Hydrodynamic constraints and storm wave characteristics on a sub-horizontal shore platform. *Earth Surface Processes and Landforms*, 40(1), 65-77. Doi:10.1002/esp.3619.
- Ogawa, H., M. E. Dickson, and P. S. Kench (2016), Generalised observations of wave characteristics on near-horizontal shore platforms: Synthesis of six case studies from the North Island, New Zealand, *New Zealand Geographer*, 72(2), 107-121. Doi: 10.1111/nzg.12121.
- Ogawa, H., M. E. Dickson, and P. S. Kench (2011), Wave transformation on a sub-horizontal shore platform, Tatapouri, North Island, New Zealand, *Continental Shelf Research*, 31(14), 1409-1419. Doi:10.1016/j.csr.2011.05.006
- Ogawa, H., M.E. Dickson, P.S. Kench, (2012). Field measurements of wave characteristics on a near-horizontal shore platform, Oraka, NZ. *Geographical Research.*, 50, 179-192.
- Pethick, J., (1984). An introduction to coastal Geomorphology. Edward Arnold, London
- Poate, T.G.; G. Masselink, M. Austin, M.E. Dickson, and P. Kench, (2016). Observations of Wave Transformation on Macro-Tidal Rocky Platforms. In: Vila-Concejo, A.; Bruce, E.; Kennedy, D.M., and McCarroll, R.J. (eds.), Proceedings of the 14th International Coastal Symposium (Sydney, Australia). Journal of Coastal Research, Special Issue, No. 75, pp. 602-606. Coconut Creek (Florida), ISSN 0749-0208.
- Raubenheimer, B., R. T. Guza, and S. Elgar (1996), Wave transformation across the inner surf zone, *Journal of Geophysical Research: Oceans*, 101(C11), 25589-25597. Doi: 10.1029/96JC02433.
- Rogers, J. S., S. G. Monismith, D. A. Kowek, and R. B. Dunbar (2016), Wave dynamics of a Pacific Atoll with high frictional effects, *Journal of Geophysical Research: Oceans*, 121(1), 350-367.
- Ruessink, B. G., G. Ramaekers, and L. C. van Rijn (2012), On the parameterization of the free-stream non-linear wave orbital motion in nearshore morphodynamic models, *Coastal Engineering*, 65, 56-63. Doi: 10.1016/j.coastaleng.2012.03.006
- Sallenger, A. H., and R. A. Holman (1985), Wave energy saturation on a natural beach of variable slope, *Journal of Geophysical Research: Oceans*, 90(C6), 11939-11944. Doi: 10.1029/JC090iC06p11939.
- Stephenson, W. J., and L. A. Naylor (2011), Geological controls on boulder production in a rock coast setting: Insights from South Wales, UK, *Marine Geology*, 283(1-4), 12-24. Doi: 10.1016/j.margeo.2010.07.001.
- Stephenson, W. J., and R. M. Kirk (2000), Development of shore platforms on Kaikoura Peninsula, South Island, New Zealand: Part One: The role of waves, *Geomorphology*, 32(1-2), 21-41. Doi: 10.1016/S0169-555X(99)00061-6.
- Sunamura, T., 1992. Geomorphology of Rocky Coasts, Wiley and Sons, New York. 302pp
- Thornton, E. B., and R. T. Guza (1983), Transformation of wave height distribution, *Journal of Geophysical Research: Oceans*, 88(C10), 5925-5938. Doi: 10.1029/JC088iC10p05925.
- Symonds, G., K. P. Black, and I. R. Young (1995), Wave-driven flow over shallow reefs, *Journal of Geophysical Research: Oceans*, 100(C2), 2639-2648. Doi: 10.1029/94JC02736.
- Trenhaile, A. S. (1987), *The geomorphology of rock coasts*, Oxford University Press, Incorporated, 384 p.



- Trenhaile, A.S., (1999). The width of shore platforms in Britain, Canada, and Japan. *Journal of Coastal Research*, 15, 355 – 364.
- Trenhaile, A. S., and J. I. Kanyaya (2007), The Role of Wave Erosion on Sloping and Horizontal Shore Platforms in Macro- and Mesotidal Environments, *Journal of Coastal Research*, 298-309. Doi: 10.2112/04-0282.1.
- Thornton, E. B., and R. T. Guza (1982), Energy saturation and phase speeds measured on a natural beach, *Journal of Geophysical Research: Oceans*, 87(C12), 9499-9508. Doi: 10.1029/JC087iC12p09499.
- van Gent, M.R.A., 2001. (2001), Wave Runup on Dikes with Shallow Foreshores, *Journal of Waterway, Port, Coastal, and Ocean Engineering*, 127(5). Doi: 10.1061/(ASCE)0733-950X(2001)127:5(254).
- Vetter, O., J. M. Becker, M. A. Merrifield, A. C. Pequignet, J. Aucan, S. J. Boc, and C. E. Pollock (2010), Wave setup over a Pacific Island fringing reef, *Journal of Geophysical Research: Oceans*, 115(C12), 1-13. Doi: 10.1029/2010JC006455
- Welch, P., (1967). The use of fast Fourier transform for the estimation of power spectra: a method based on time averaging over short, modified periodograms. *IEEE Transactions on Audio and Electroacoustics* 15 (2), 70 – 73.
- Wright, L. D., P. Nielsen, A. D. Short, and M. O. Green (1982), Morphodynamics of a macrotidal beach, *Marine Geology*, 50(1-2), 97-127.
- Table 1 – Summary data for each deployment site; PT = Pressure sensor, ODN = Ordnance datum Newlyn,  $\tan\beta$  = slope along PT array,  $H_s$  = significant wave height,  $T_p$  = peak wave height,  $H_b$  = breaker wave height,  $h_b$  = breaker water depth.

Parameters		Sites					
		DOL	FWR	FWB	LST	HLQ	PTW
Deployment Data	Duration (tides)	13	8	8	8	12	8
	# PTs	15	14	5	15	12	12
	# Vectors	2	2	0	2	2	2
	PT spacing (m)	~10	~10	~15	~15	~10	~15
	PT z range m ODN (min, max)	-1.77, 1.66	-0.67, 2.12	-1.64, -0.95	-1.46, 3.14	-1.82, 0.46	-1.9, 2.35
	PT x range (m)	100	150	60	225	115	170
	Video (hrs)	32	36	36	11	38	19
Platform Morphology	Intertidal platform width (m)	160	210	210	325	140	180
	Bedrock	Limestone	Sandstone	n/a	Mudstone	Sandstone/shale	Slate/siltstone
	Average $\tan\beta$ between PT s	0.031	0.018	0.011	0.021	0.030	0.028
	Roughness (alongshore average, $k_\sigma / k_R$ )	0.072/0.020	0.144/0.062	0.008/0.002	0.068/0.015	0.104/0.029	0.172/0.090
	Mean spring tide range (mODN), mean low water spring (mODN)	4.2, 0.2	6.4, -3.1	6.4, -3.1	10.7, -5	7.3, -4.1	4.5, -2.1
Hydrodynamics	$H_s$ (min, max)	0.30, 1.87	0.52, 2.69	0.35, 3.03	0.11, 1.75	0.65, 1.60	0.42, 1.71
	$T_p$ (min, max)	8.94, 17	8.37, 16	8.2, 15.5	5.8, 9.4	7.5, 10.1	7.3, 13.9

	$H_b$ (min, max)	0.73, 1.65	1.66, 2.37	1.83, 2.46	0.55, 1.56	1.08, 1.56	0.72, 1.04
	$h_b$ (min, max)	1.73, 3.36	3.49, 4.04	4.30, 5.09	2.19, 3.52	3.52, 4.35	4.17, 4.48
	$H^2T_p$ (min, max)	5.1, 43.8	28.4, 107.2	33.0, 134.4	6.8, 22.8	9.7, 18.41	4.0, 22.3

950

951 Table 2 – Summary of platform gradient ( $\tan\beta$ ), roughness length-scale ( $k_\sigma$ ) and empirical drag  
 952 coefficient ( $C_{f,Nielsen}$ ; **Eq. 17**), and numerical model short-wave dissipation parameters, averaged over  
 953 four tidal cycles for all field sites. Model parameters are: optimised drag coefficient ( $C_f$ ), rms and  
 954 significant breaker criterion ( $\gamma$ ), ratio of frictional to breaker dissipation ( $\langle\epsilon_f/\epsilon_b\rangle$ ), and wave height to  
 955 water depth ratio ( $H_{s,inc}/h$ ).

	Observed			Computed				
	$\tan\beta$	$k_\sigma$	$C_{f,Nielsen}$	$C_f$	$\gamma_{rms}$	$\gamma_s$	$\langle\epsilon_f/\epsilon_b\rangle$	$H_{s,inc}/h$
<b>DOL</b>	0.031	0.072	0.0367	0.0502	0.36	0.51	0.142	0.69
<b>FWR</b>	0.018	0.144	0.0388	0.0005	0.53	0.71	0.002	0.68
<b>LST</b>	0.021	0.068	0.0225	0.0005	0.60	0.84	0.002	0.68
<b>HLQ</b>	0.03	0.104	0.0336	0.049	0.44	0.62	0.140	0.61
<b>PTW</b>	0.028	0.172	0.0690	0.3413	0.66	0.93	3.820	0.54

956

957 Figure 1 – Effect of varying  $\gamma$  and  $C_f$  for wave transformation over a plane-sloping bed with  $\tan\beta =$   
 958 0.02 according to [Thornton and Guza \(1982\)](#) model. (a) Seabed gradient (solid line) and still water-  
 959 level (dashed line). (b – d)  $H_s$ ,  $\epsilon_b$  and  $H_s/h$  for values of  $\gamma$  varied through the range indicated in the  
 960 colorbar with  $C_f = 0.01$ . (e – g)  $H_s$ ,  $\epsilon_f$  and  $H_s/h$  for values of  $C_f$  shown in the colourbar and  $\gamma = 0.42$ .

961 Figure 2 – Location maps and aerial images of the five field sites; (a) Doolin (DOL), (b) Freshwater  
 962 West (FWR & FWB), (c) Lilstock (LST), (d) Hartland Quay (HLQ) and (e) Portwrinkle (PTW).

963 Figure 3 – Cross-shore profiles for each of the field sites with locations of pressure transducers (black  
 964 dots). The vertical bar in each of the panels represents the mean spring tidal range.

965 Figure 4 – Example identification of shoaling wave and surf zone conditions at Hartland Quay. (a)  
 966 Rectified and merged video images across the shore platform with sensor locations (red dots) overlaid  
 967 to identify regions of breaking (white) and shoaling waves (grey). (b) All data with water depth ( $h$ )  
 968 plotted versus significant wave height ( $H_s$ ) with blue and yellow symbols representing surf zone and  
 969 shoaling waves, respectively. Red symbols represent the wave conditions coincident in (a). (c) Spatial  
 970 and temporal variability in  $H_s$  for a single tidal cycle, with color scale running from 0.2 m (dark blue)  
 971 to 1.4 m (yellow). Dashed line represent demarcation of the surf zone and the video image in (a)  
 972 corresponds to the time 15:50 hrs (solid line).

973 Figure 5 – De-trended digital elevation models (DEMs) with PT locations (black circles) for all study  
 974 sites with colour scale running from -1 (dark blue) and +1 m (yellow). Offshore is at the top of the  
 975 DEMs. The two lines to the right of the DEMs represent the cross-shore variation in the alongshore-  
 976 averaged roughness based on standard deviation  $k_\sigma$  and rugosity  $k_R$ .

977 Figure 6 – Time series of the significant wave height ( $H_s$ ; solid line) and wave period ( $T_{spec}$ ; dashed  
 978 line) for each of the sites recorded by the nearest offshore wave buoy. Symbols (black circles)  
 979 represent the tide-averaged significant breaker height for each of the monitored tides estimated from  
 980 the pressure sensors deployed across the shore platforms.

981 Figure 7 – Left panels show incident significant wave height ( $H_s$ ) versus normalised surf zone  
 982 position ( $h/h_b$ ) for all data runs with colour of the symbols representing the breaker height ( $H_b$ ), with  
 983 the colour bar running from 0.5 m (blue) to 3 m (yellow). Right panels show boxplots of relative wave  
 984 height ( $H_{s,inc}/h$ ) versus normalised surf zone position ( $h/h_b$ ). On each box, the central mark (red line) is  
 985 the median, the edges of the box are the 25th and 75th percentiles, the whiskers extend to the most

extreme data points not considered outliers ( $< 0.4^{\text{th}}$  percentile or  $> 99.6^{\text{th}}$  percentile). The dashed line indicates the edge of the surfzone.

Figure 8 – Observed average (solid circles) and standard deviation (vertical bars) of  $H_{\text{sync}}/h$  versus normalised platform/beach slope ( $\tan\beta/kh$ ) for all runs broken down for the different shore platform sites. The data are binned corresponding to  $\pm 0.025$ . The dashed line represents the prediction according to [Raubenheimer et al. \(1996\)](#) represented by Eq. (1).

Figure 9 – Boxplots of wave skewness ( $A_{\text{skew}}$ ; left panels) and wave asymmetry ( $A_{\text{asym}}$ ; right panels) versus normalised surf zone position ( $h/h_b$ ). On each box, the central mark (red line) is the median, the edges of the box are the 25th and 75th percentiles, the whiskers extend to the most extreme data points not considered outliers ( $< 0.4^{\text{th}}$  percentile or  $> 99.6^{\text{th}}$  percentile).

Figure 10 – Wave skewness ( $A_{\text{skew}}$ ) and asymmetry ( $A_{\text{asym}}$ ) as a function of the Ursell number ( $Ur$ ) derived from  $H_s$ . The gray dots are the individual estimates, the filled circles are the class mean values based on binning the estimates according to  $\log(Ur) \pm 0.05$ . The vertical lines represent class standard deviation for each bin. The dashed line shows the fits proposed by [Ruessink et al. \(2012\)](#).

Figure 11 – Left panels show significant infragravity wave height ( $H_{s,\text{inf}}$ ) versus normalised surf zone position ( $h/h_b$ ) for all data runs with colour of the symbols representing the breaker height ( $H_b$ ), with the colour bar running from 0.5 m (blue) to 3 m (yellow). Right panels show boxplots of percentage of infragravity energy ( $\%Ig$ ) versus normalised surf zone position ( $h/h_b$ ). On each box, the central mark (red line) is the median, the edges of the box are the 25th and 75th percentiles, the whiskers extend to the most extreme data points not considered outliers ( $< 0.4^{\text{th}}$  percentile or  $> 99.6^{\text{th}}$  percentile).

Figure 12 – Scatter plot between the significant total infragravity wave height ( $H_{\text{inf}}$ ) near the shoreline as a function of an incident wave power factor ( $H_o^2 T_p$ ). Each data point is a tide-averaged value where  $0 < h/h_b < 0.33$ . The dashed line represents  $H_{\text{inf}} = 0.004 H_o^2 T_p + 0.20$  from [Inch et al. \(2016\)](#).

Figure 13 – Summary statistics for each site (all valid tides); (a)  $H_{s,\text{inc}}/h$ , (b) percentage infragravity energy ( $\%Ig$ ), (c) wave skewness ( $A_{\text{skew}}$ ) and (d) wave asymmetry ( $A_{\text{asym}}$ ). Circles are mean values and vertical bars represent the 95 % confidence interval ( $= t(df) \times \sigma/\sqrt{n}$ , where  $t$  is the t-statistic for the relevant degrees of freedom  $df$  and  $n$  is the number of observations).

Figure 14 – Results of model calibration for  $C_f$ , with (left)  $\epsilon_{\text{abs}}$  and (right)  $\epsilon_{\text{bias}}$ . Black lines plot the mean error distribution over  $C_f$ -space over the four calibration tidal cycles with the shaded regions indicating the range. The black triangle is the tide-mean optimised  $C_f$  with 1 standard deviation plotted as the black horizontal error bar. The black dots indicate the final optimised  $C_f$  value for each field site. The grey horizontal line in the right-hand panels indicates zero bias.

Figure 15 – Results of model calibration for  $\gamma$ , with (left)  $\epsilon_{\text{abs}}$  and (right)  $\epsilon_{\text{bias}}$ . Black lines plot the mean error distribution over  $\gamma$ -space over the four calibration tidal cycles with the shaded regions indicating the range. The black triangle is the tide-mean optimised  $\gamma$  with 1 standard deviation plotted as the black horizontal error bar. The black dots indicate the final optimised  $\gamma$  value for each field site. The grey horizontal line in the right-hand panels indicates zero bias.

Figure 16 – Example model runs for each field site (lines) compared to field observations (triangles). (Bottom) Measured and modelled  $H_s$  indicating rms error. (Centre) Total wave energy dissipation, with predicted dissipation partitioned into  $\epsilon_b$  (dash-dot line) and  $\epsilon_f$  (red dashed line). (Top) Relative wave height  $H_s/h$ , indicating the model  $\gamma$  value (dotted line). Note different x-axis scales.

Figure 17 – The behaviour of  $\epsilon_f$  as a function of (a)  $H_o$ , (b)  $\tan\beta$  and (c)  $C_f$ . Black curves (left axes) plot the  $\% \epsilon_f$  and red curves (right axes) plot the sum total  $\epsilon_f$  across the inter-tidal region.  $\gamma$  was fixed at 0.5.



Figure 1.

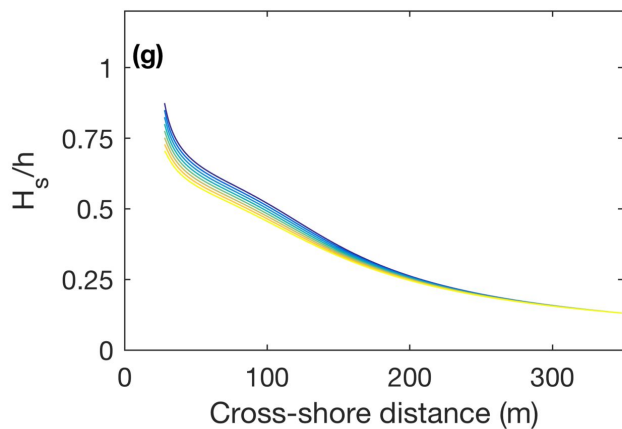
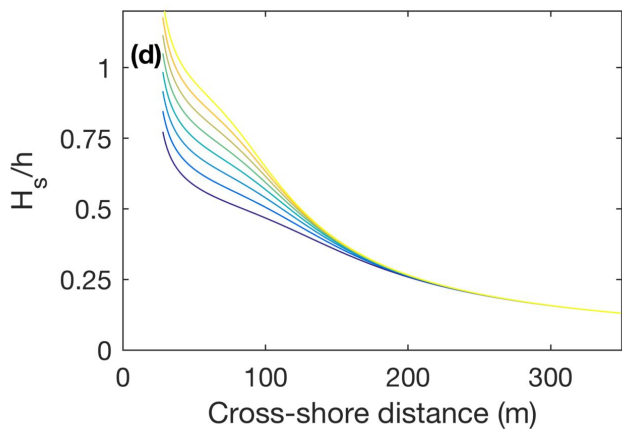
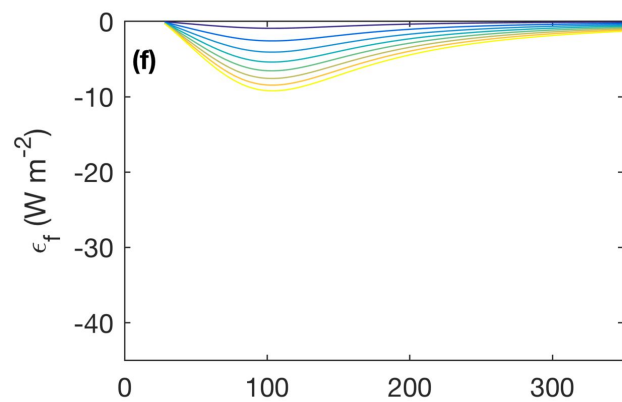
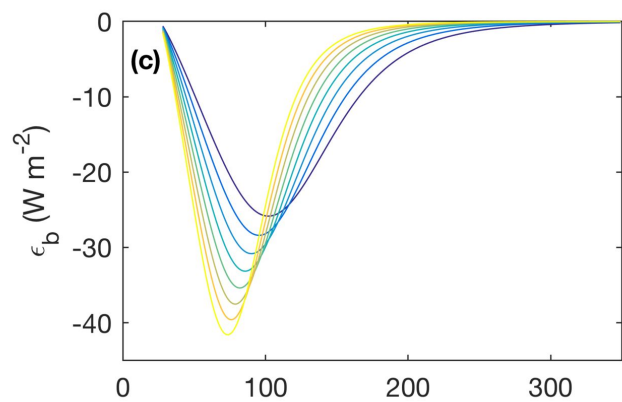
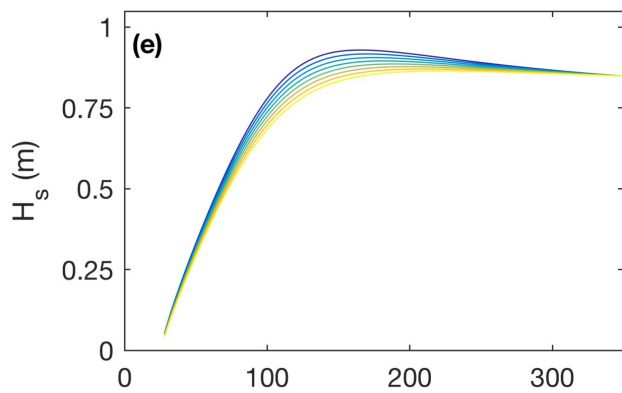
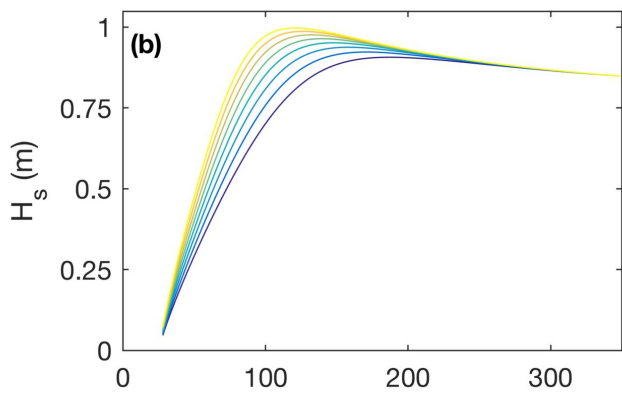
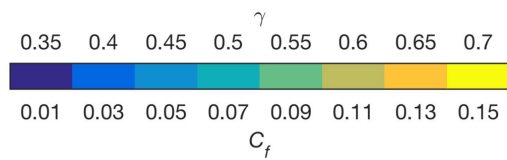
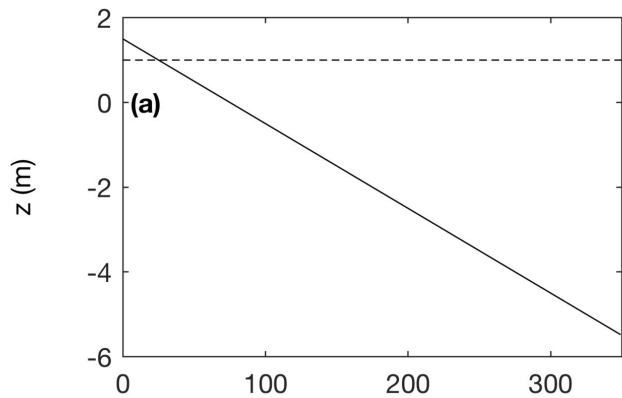


Figure 2.

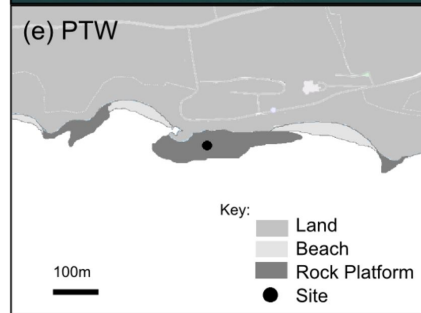
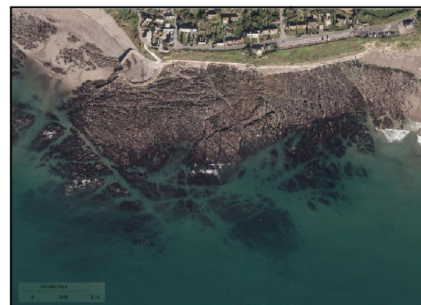
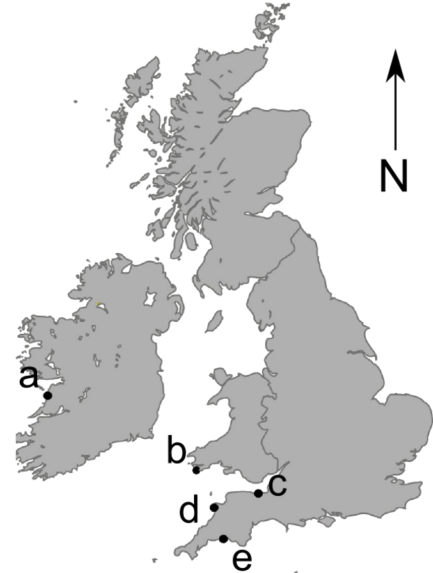
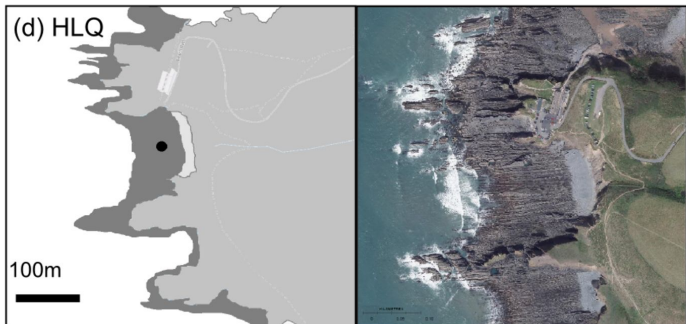
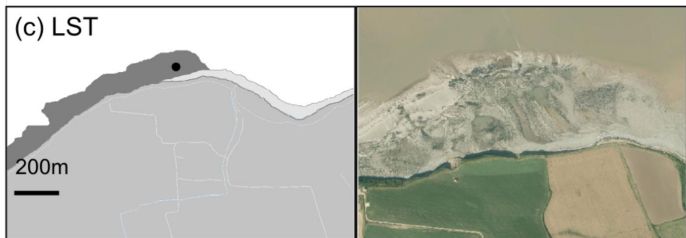
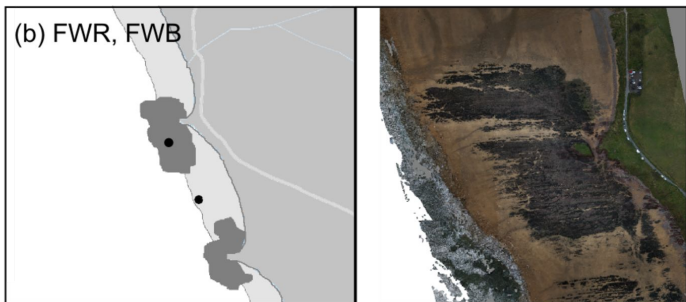




Figure 3.

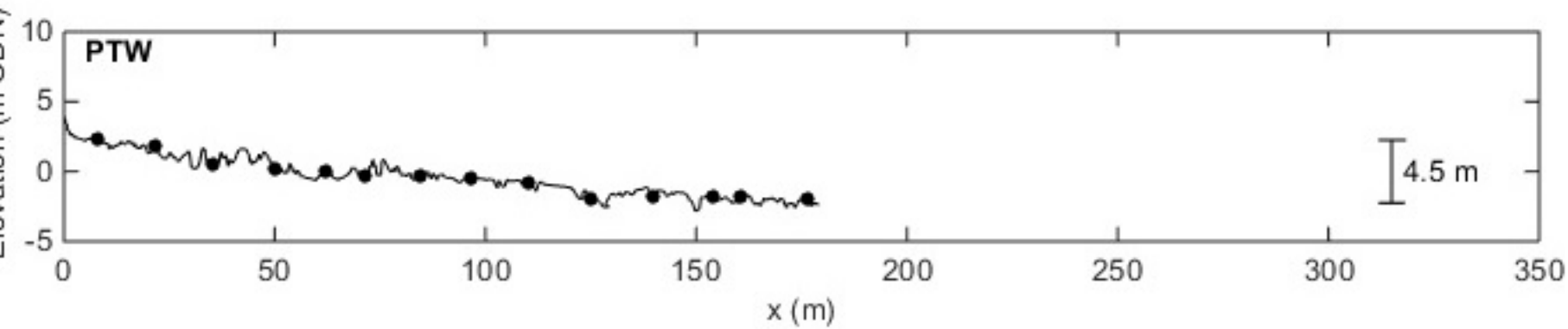
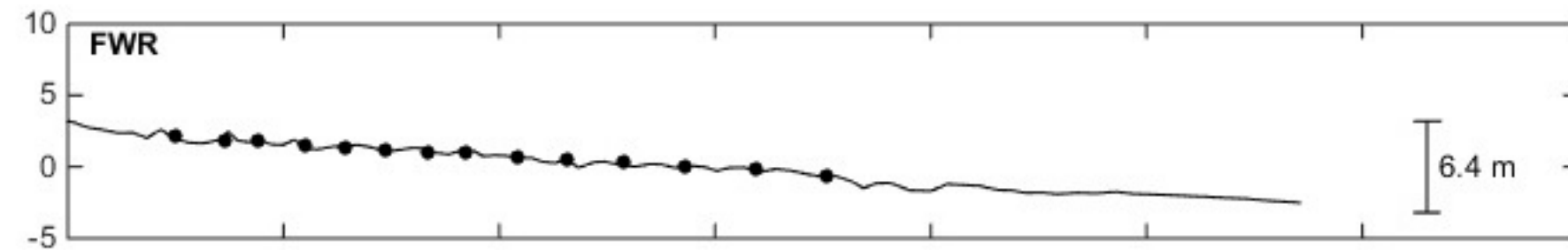
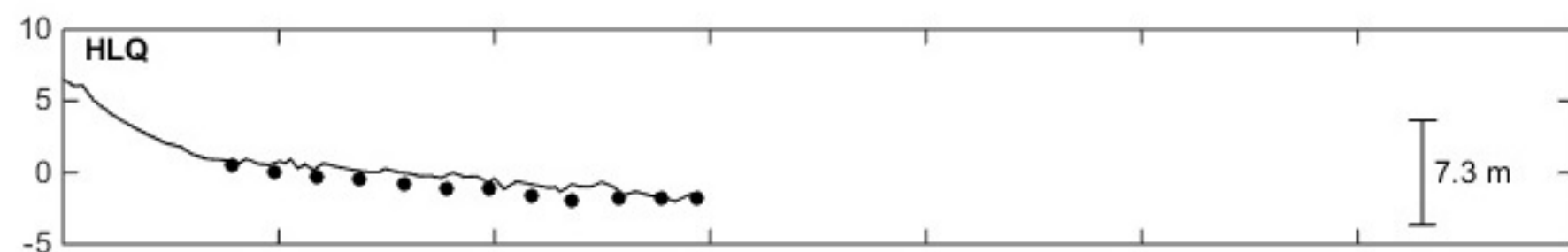
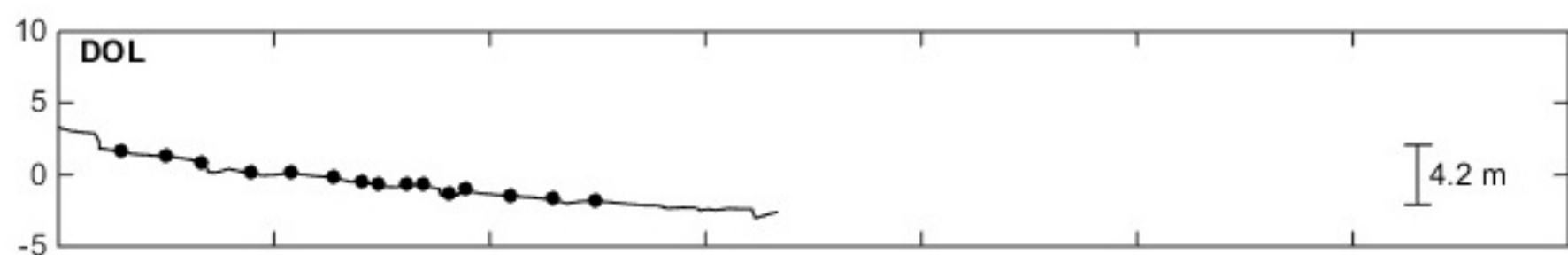
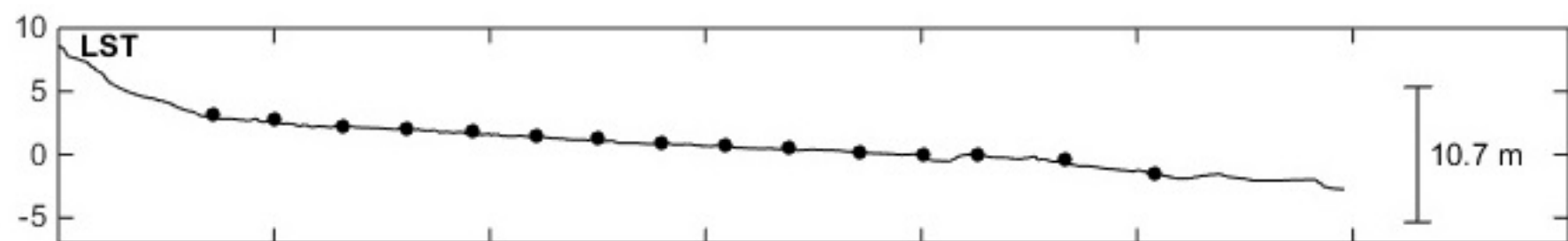
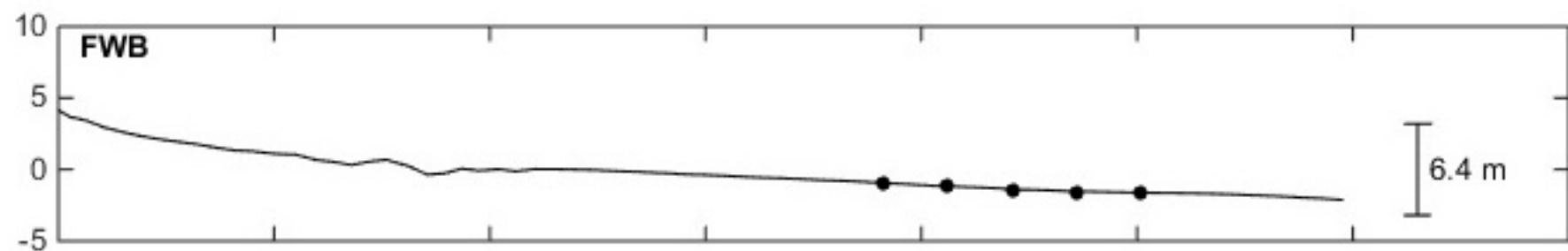


Figure 4.

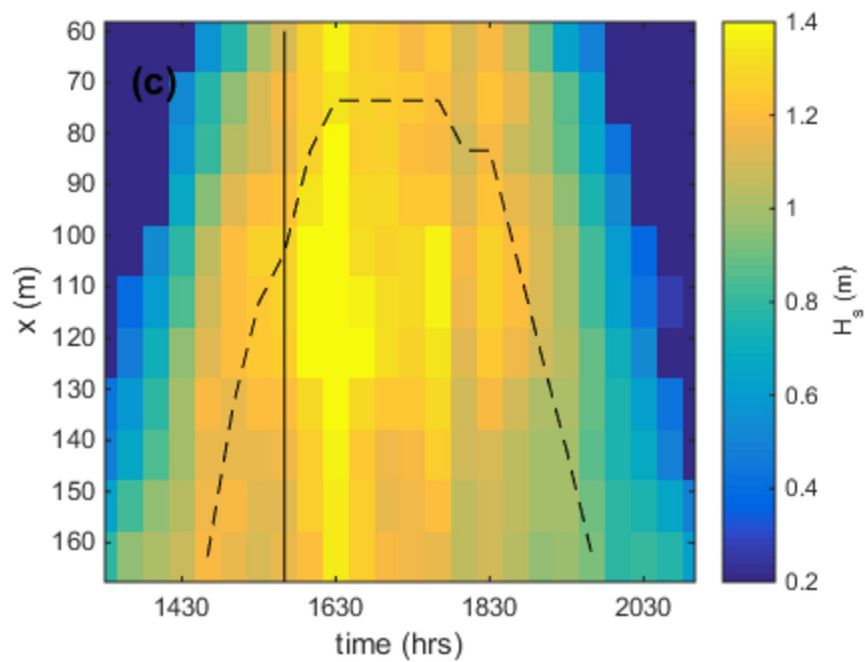
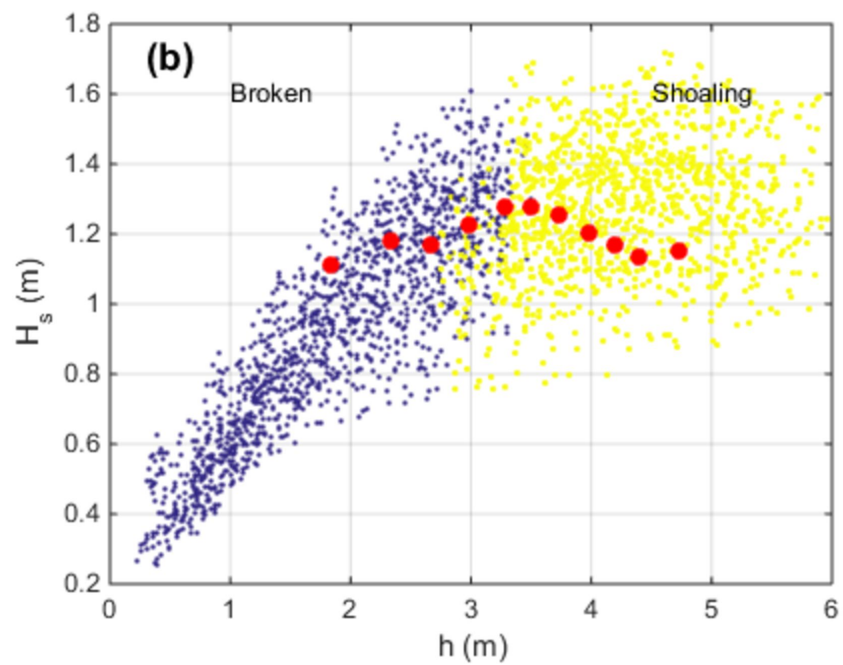
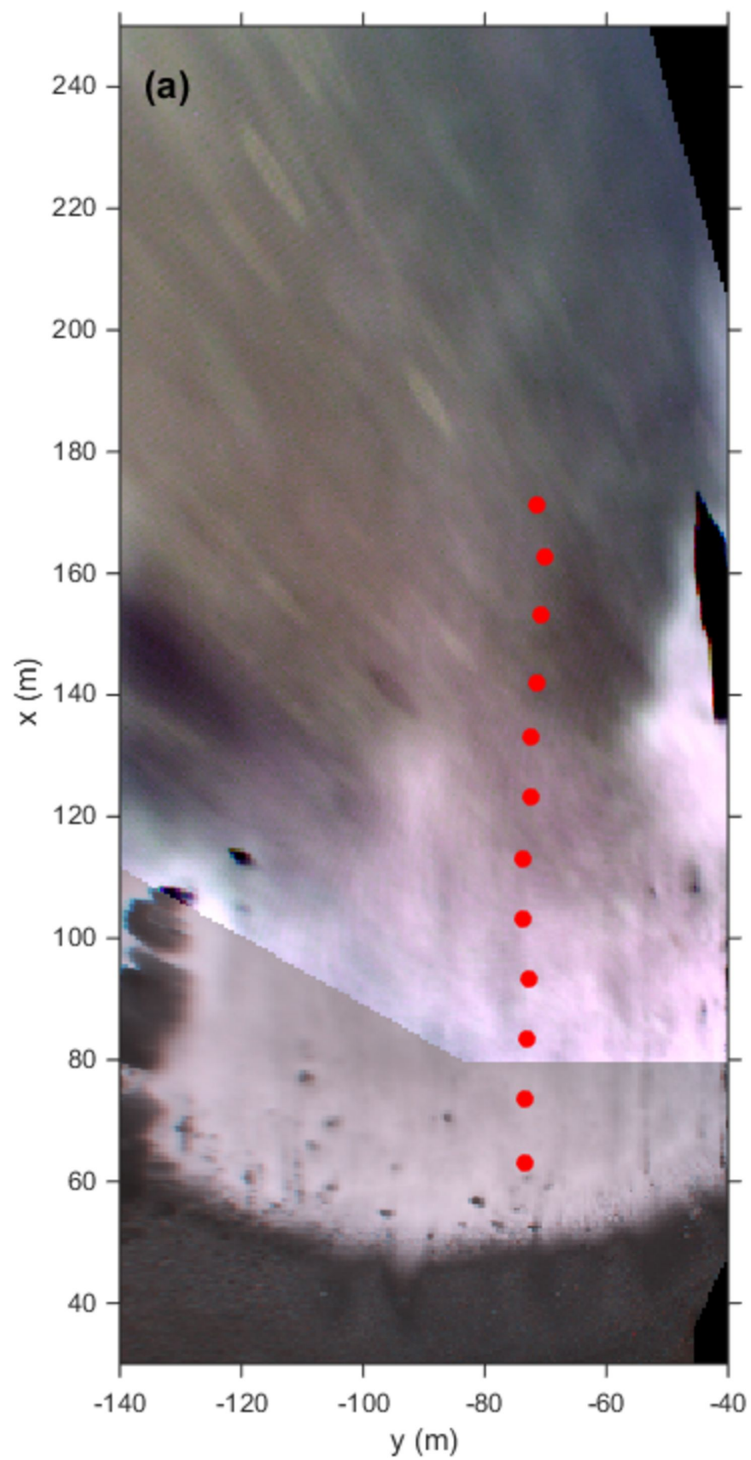


Figure 5.

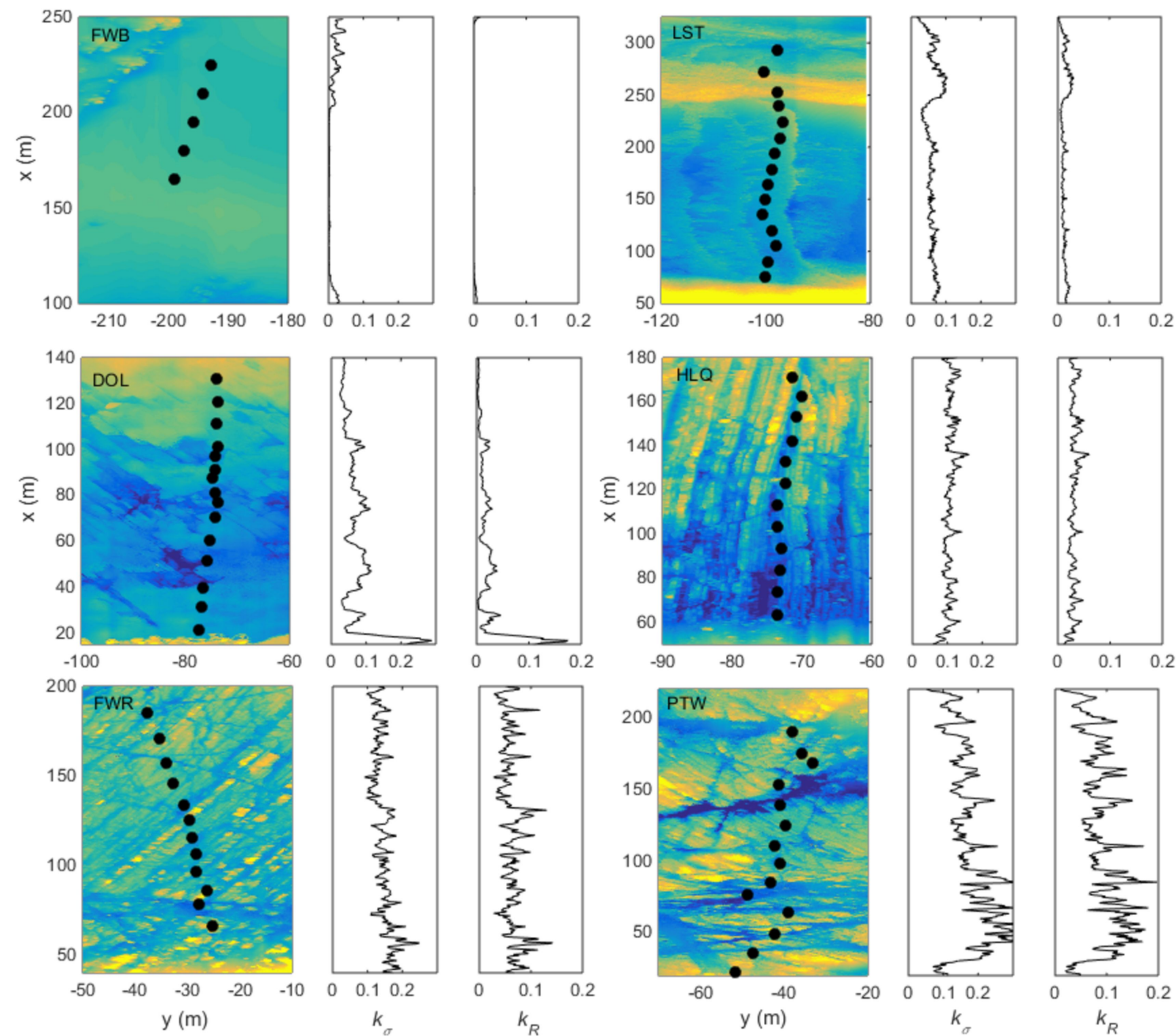
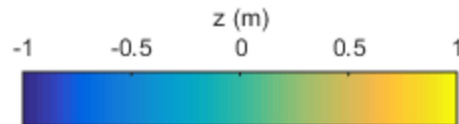


Figure 6.

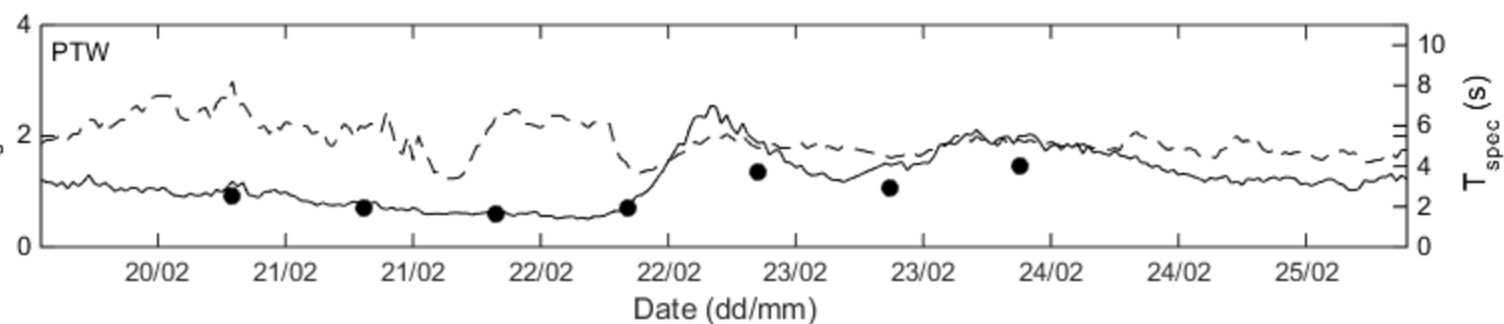
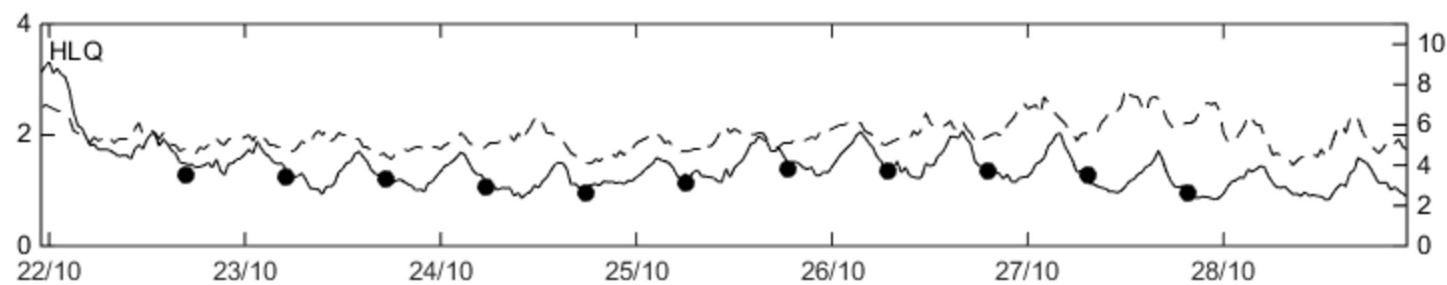
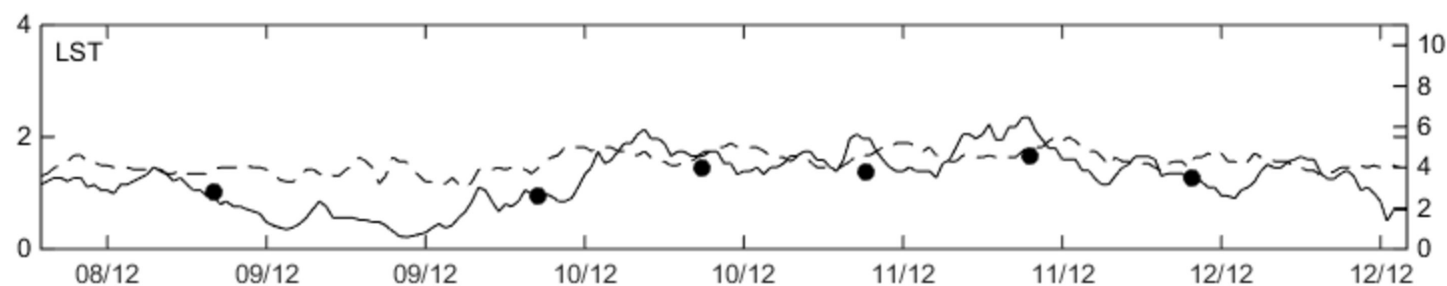
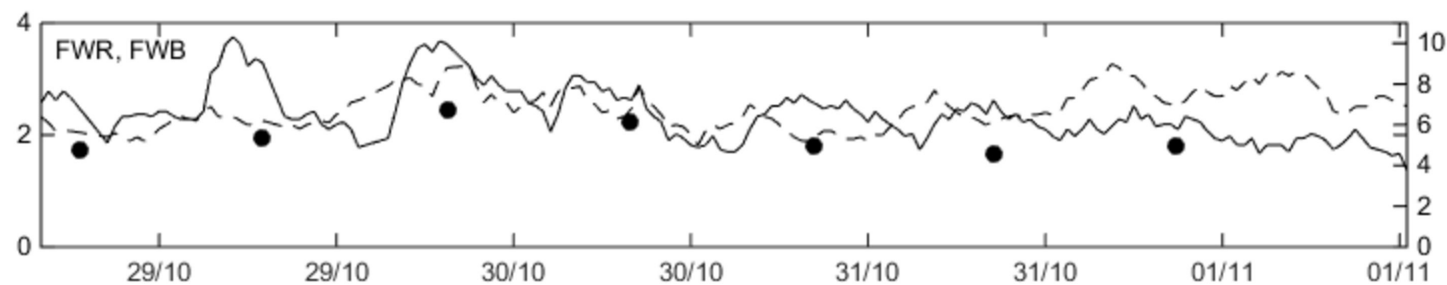
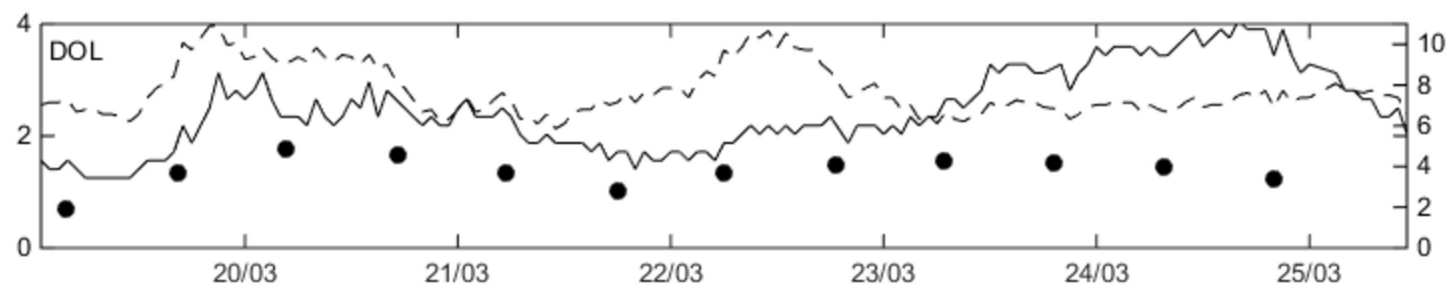




Figure 7.

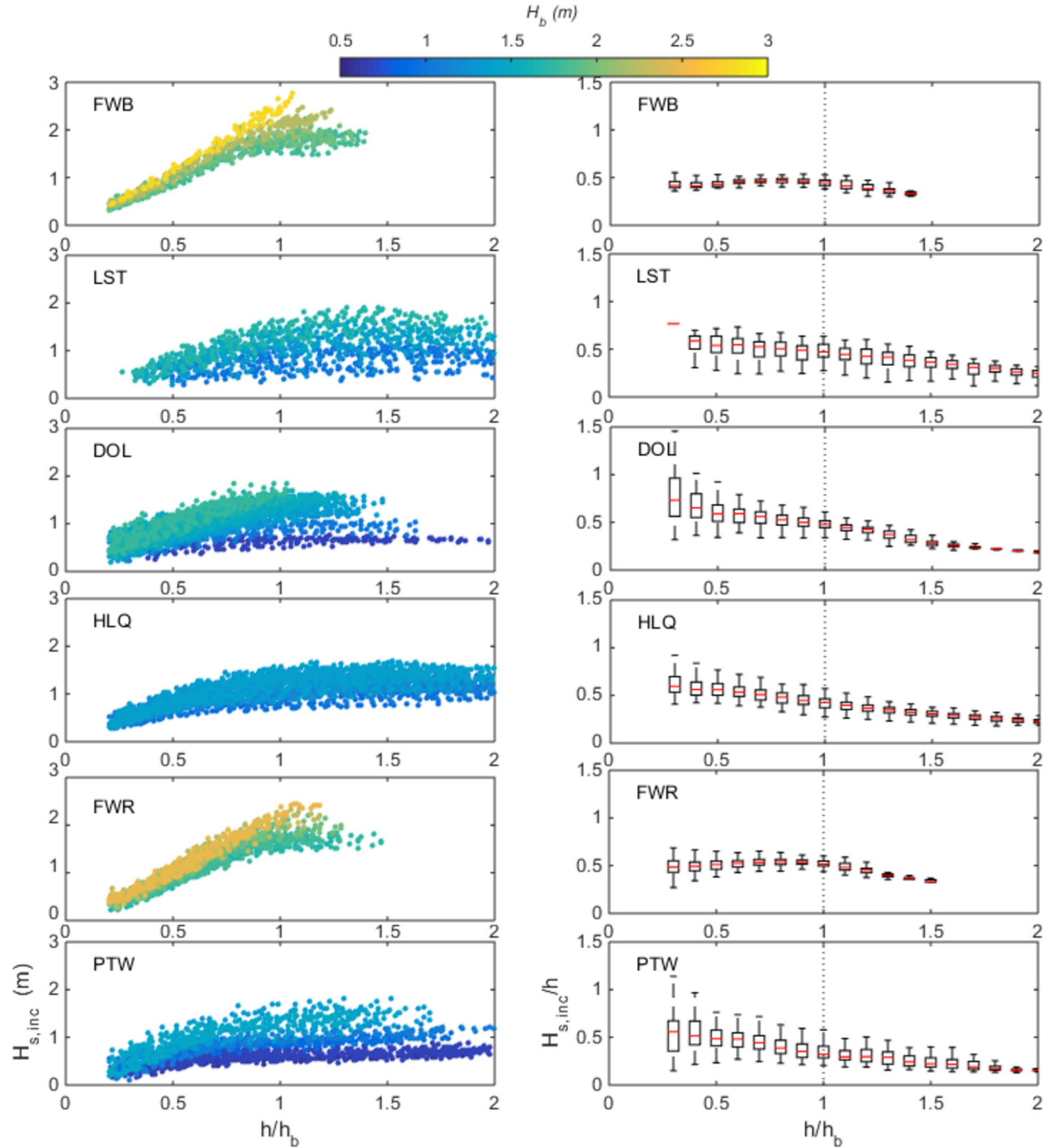


Figure 8.

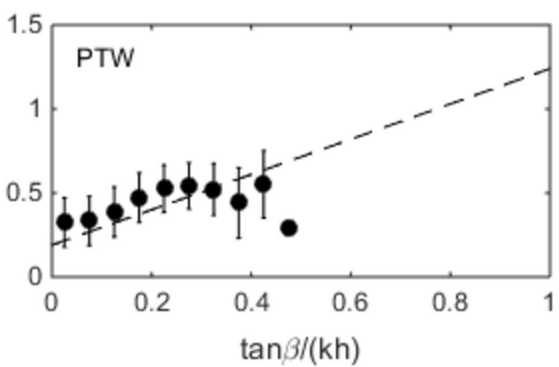
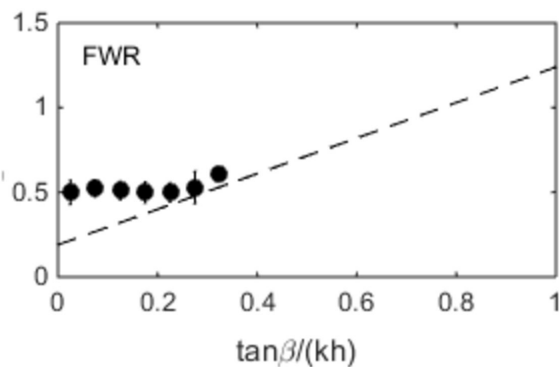
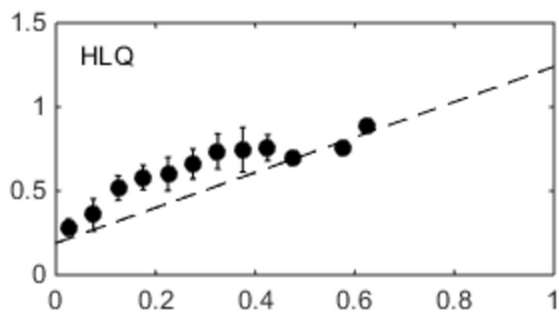
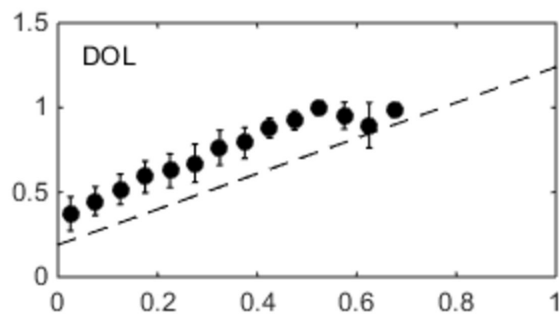
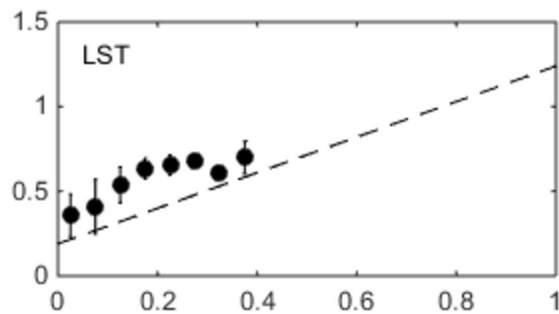
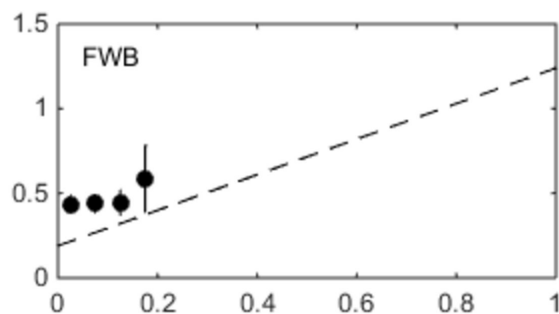


Figure 9.

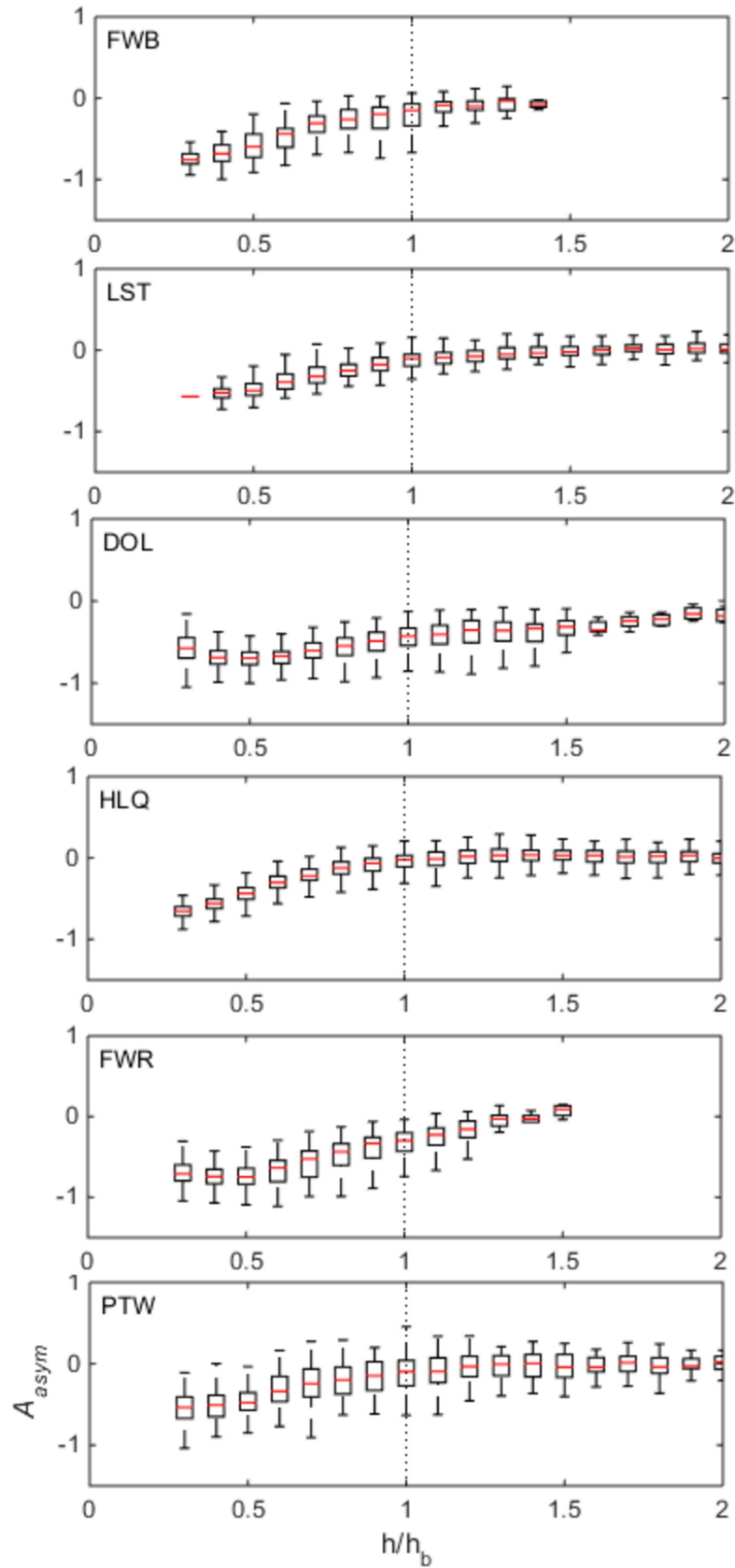
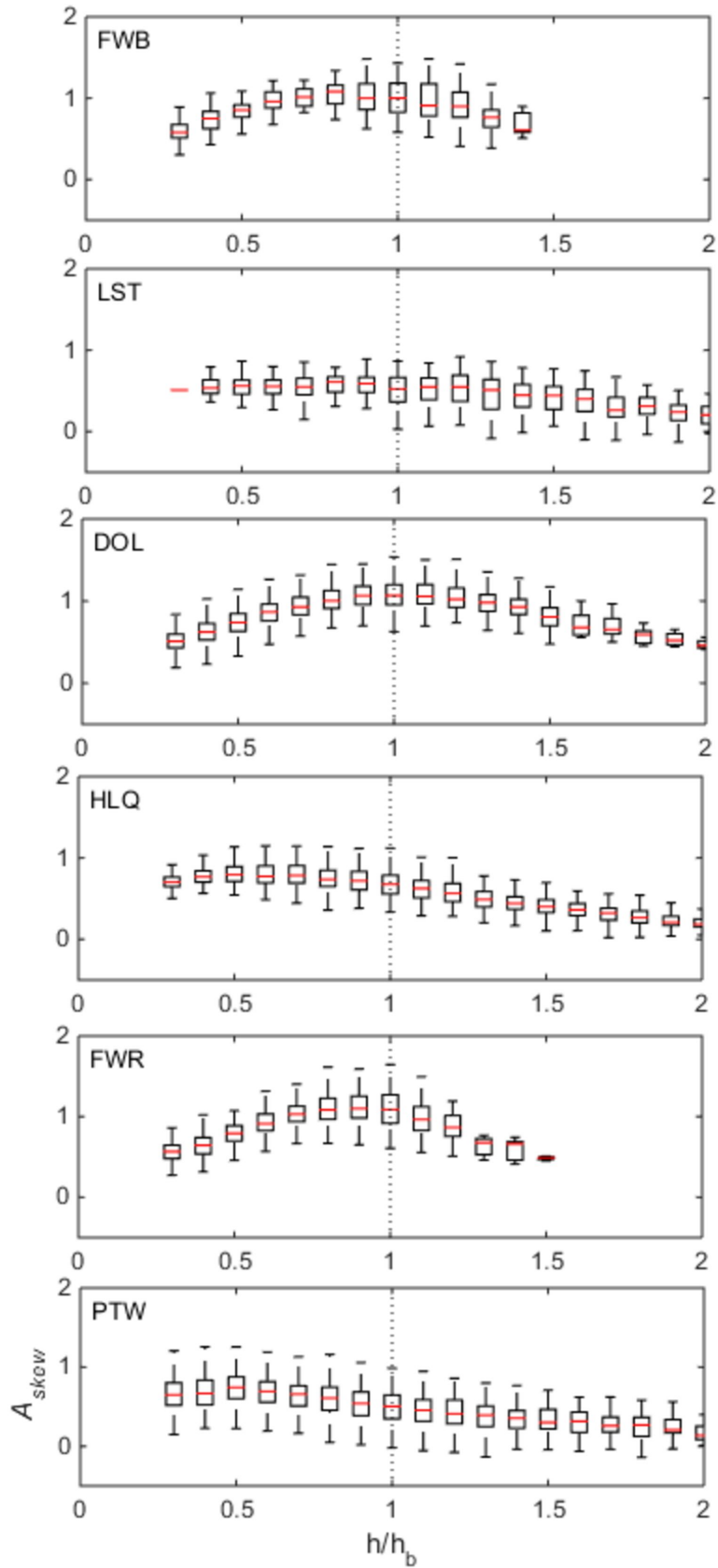




Figure 10.

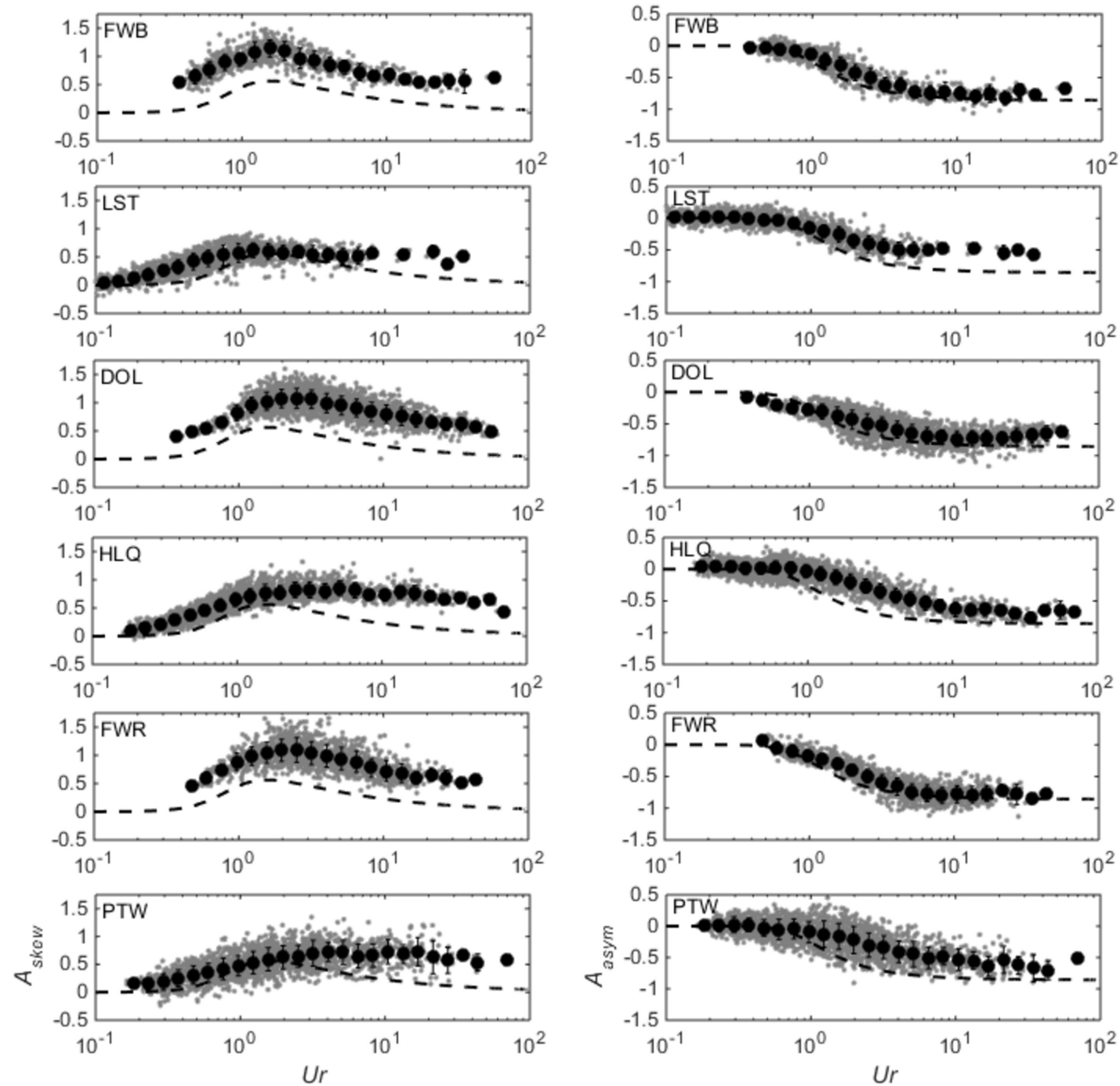


Figure 11.

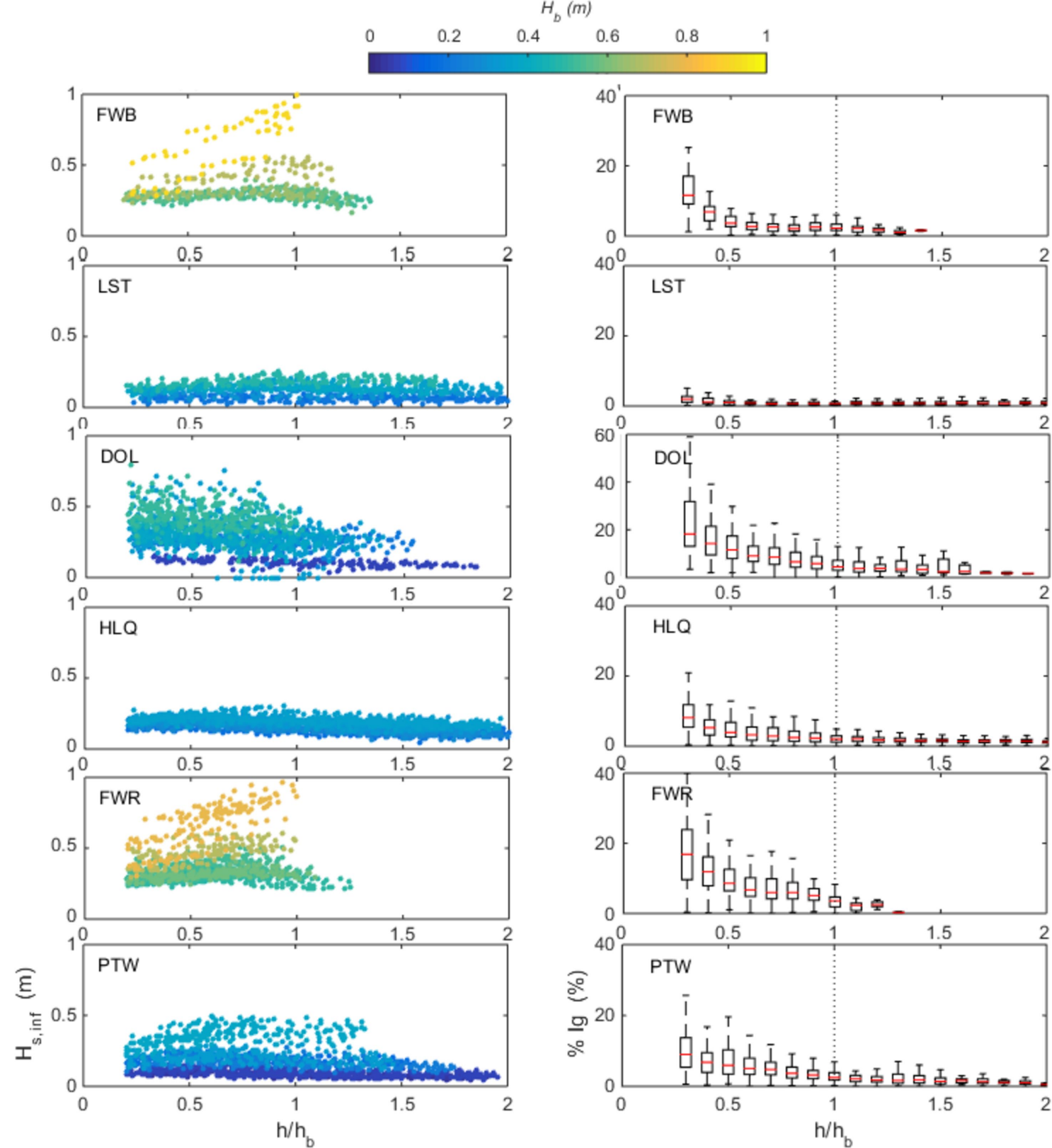


Figure 12.

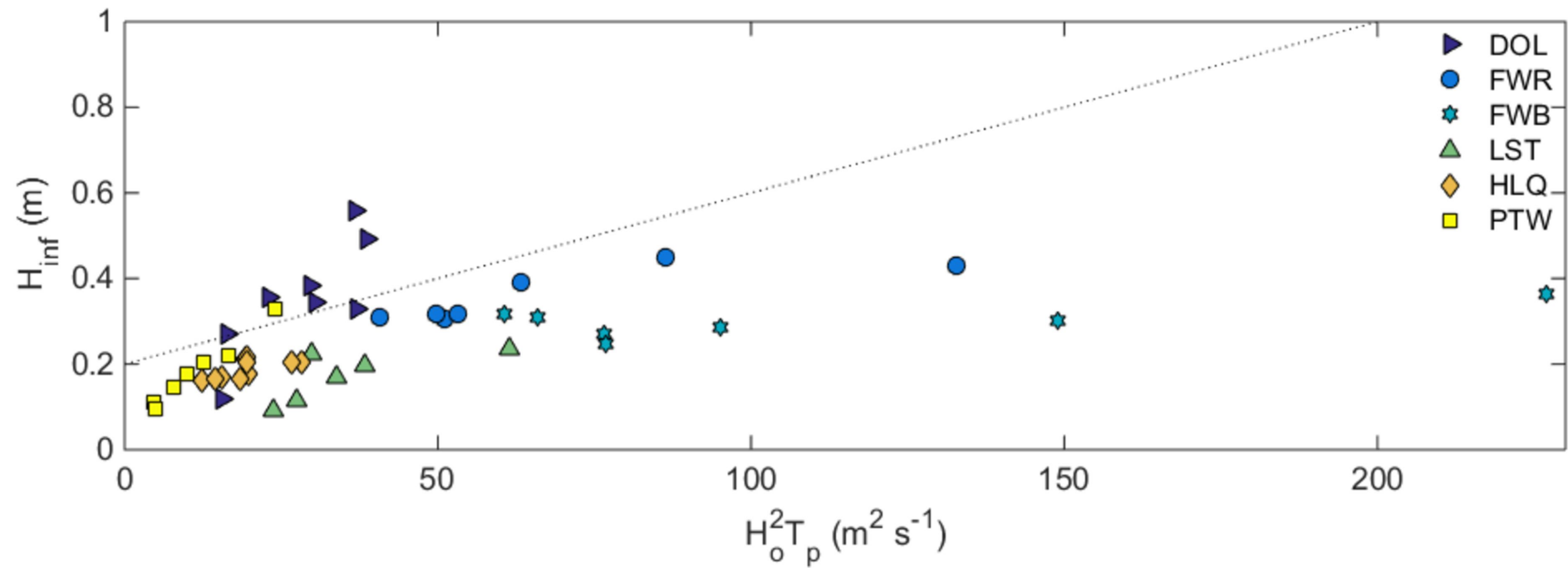




Figure 13.

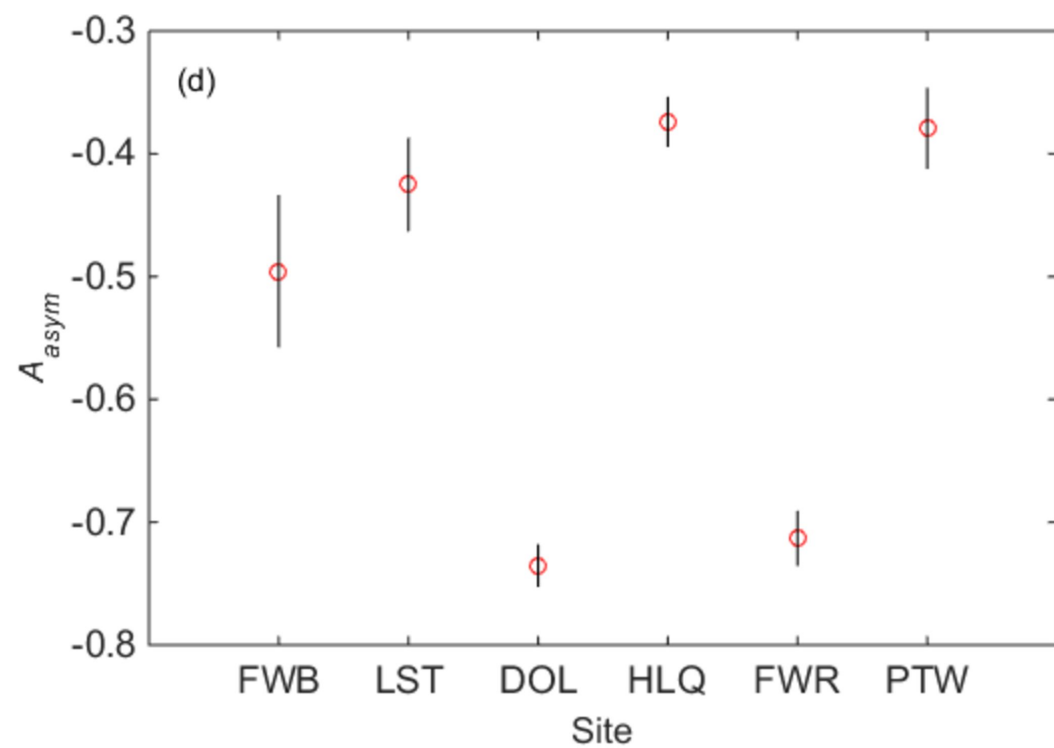
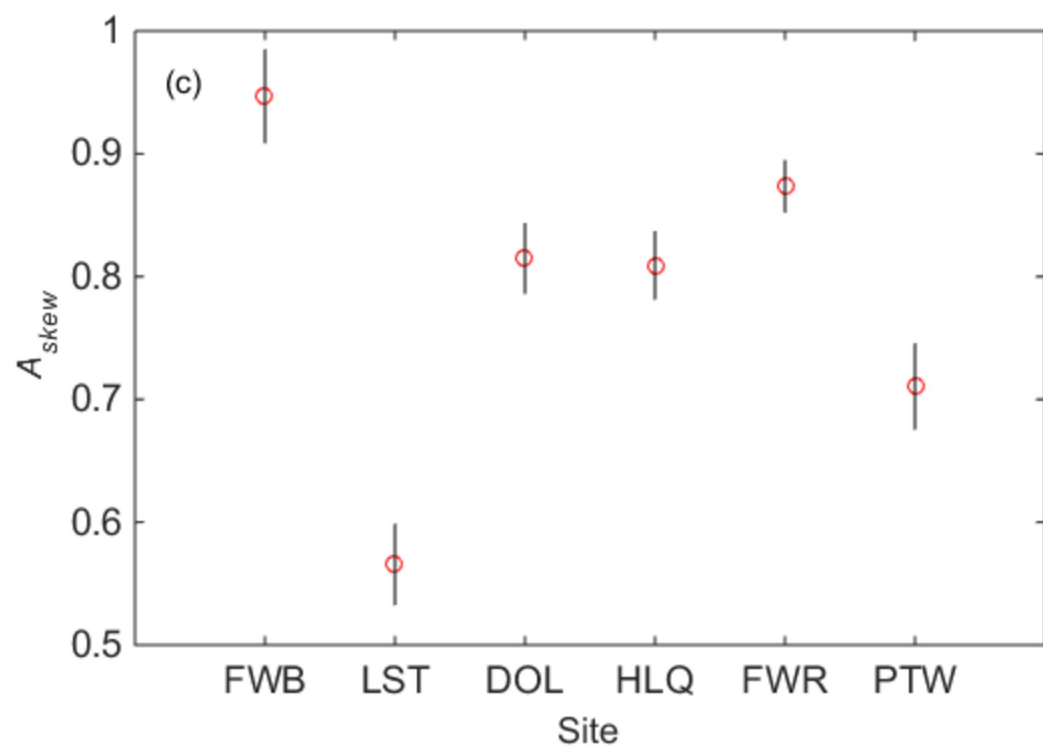
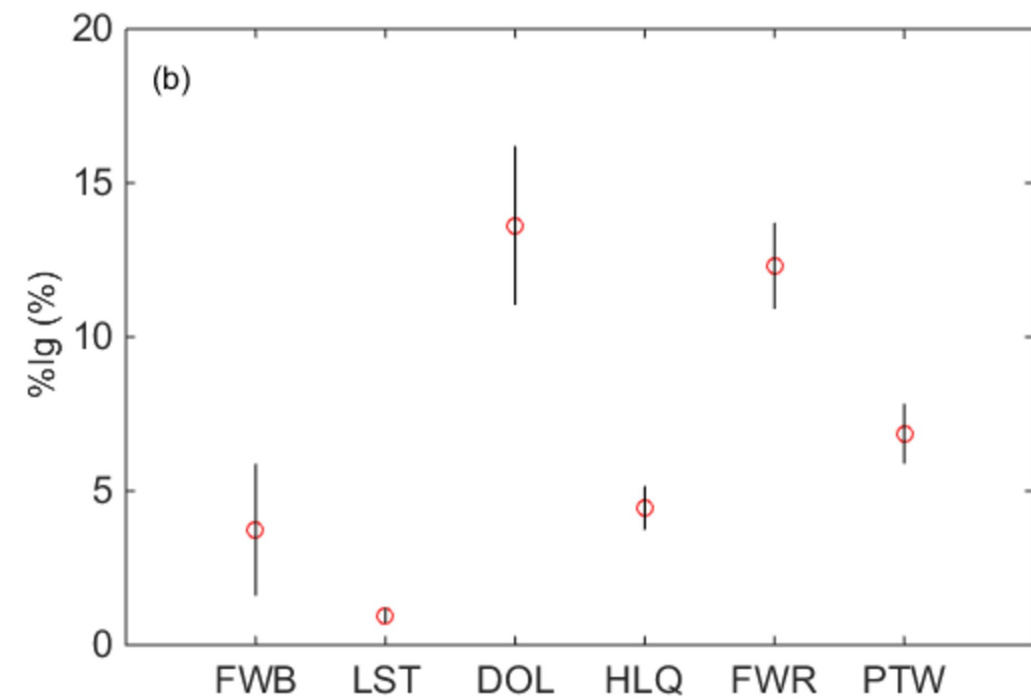
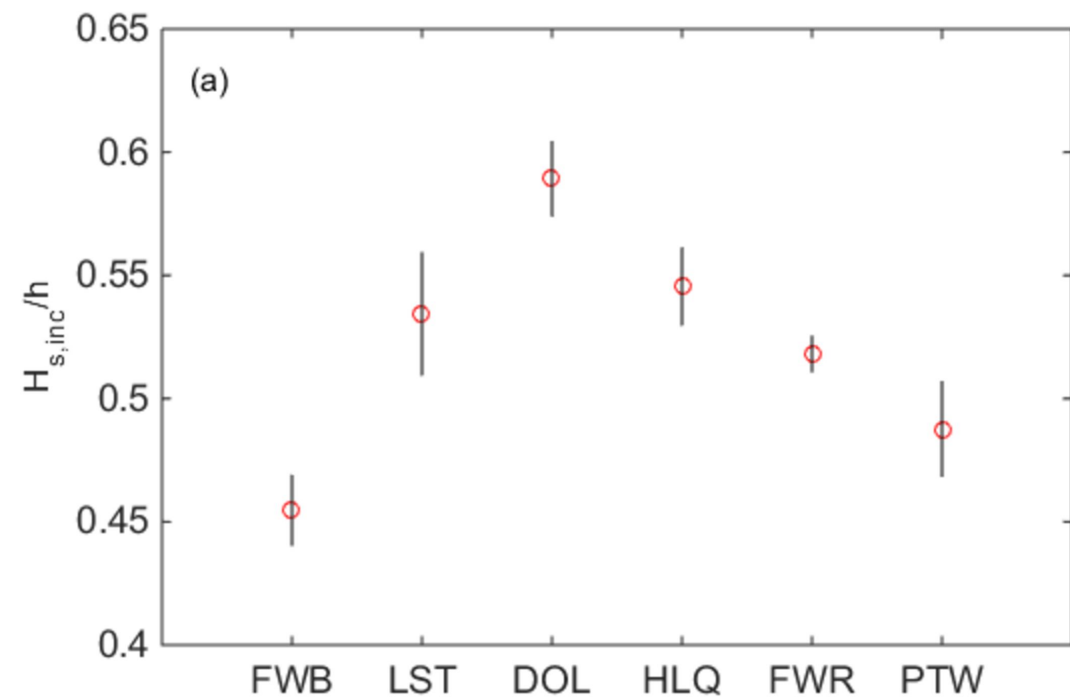


Figure 14.

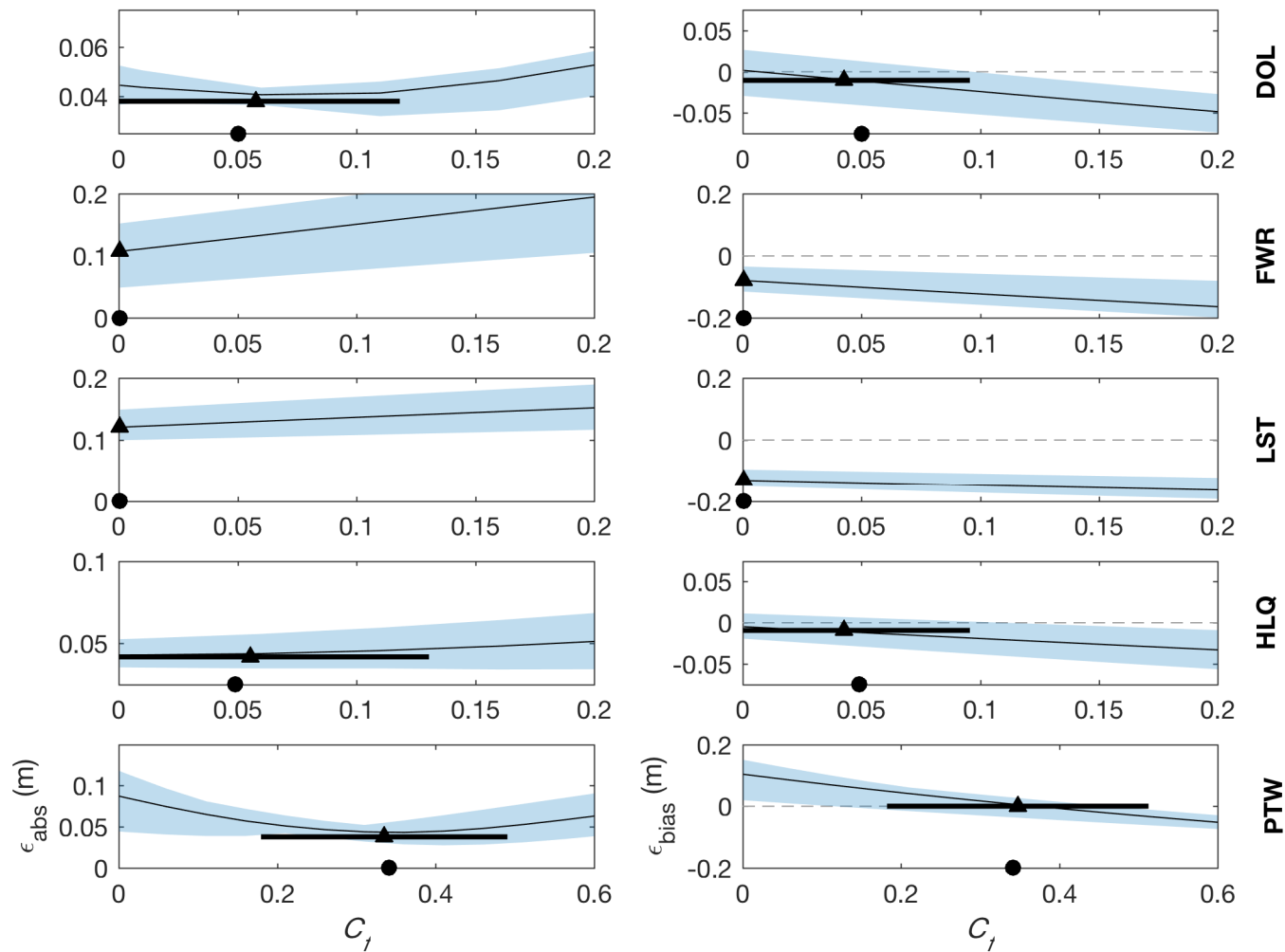


Figure 15.

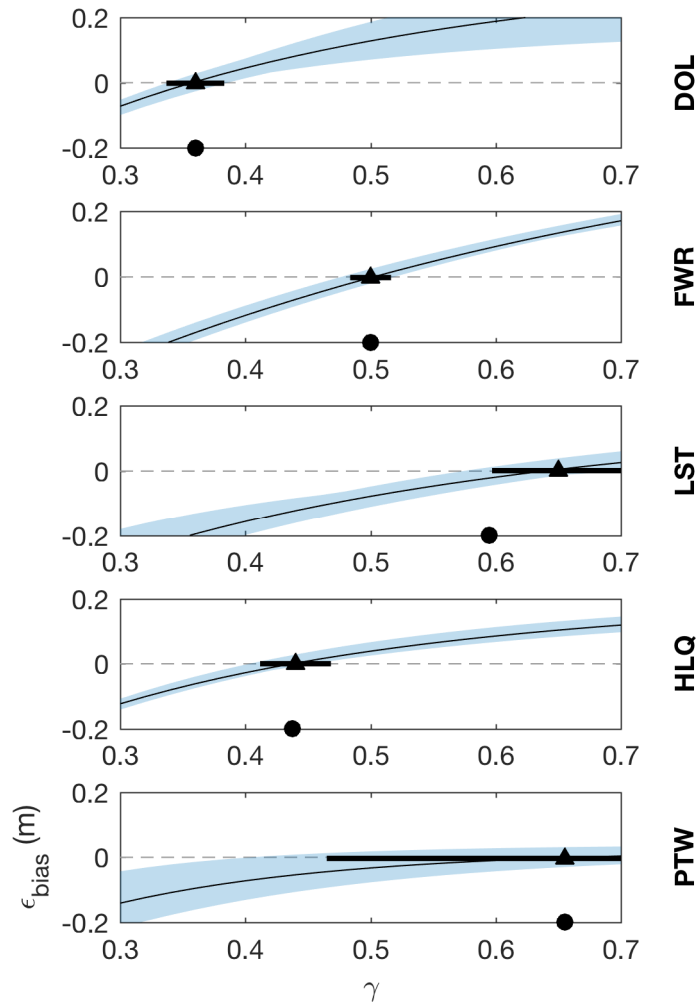
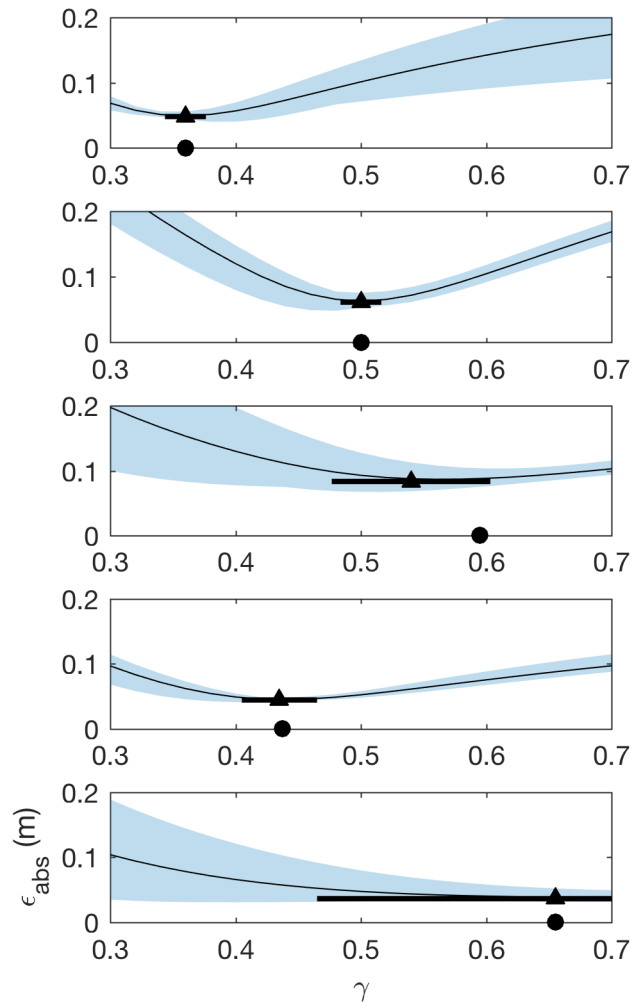


Figure 16.



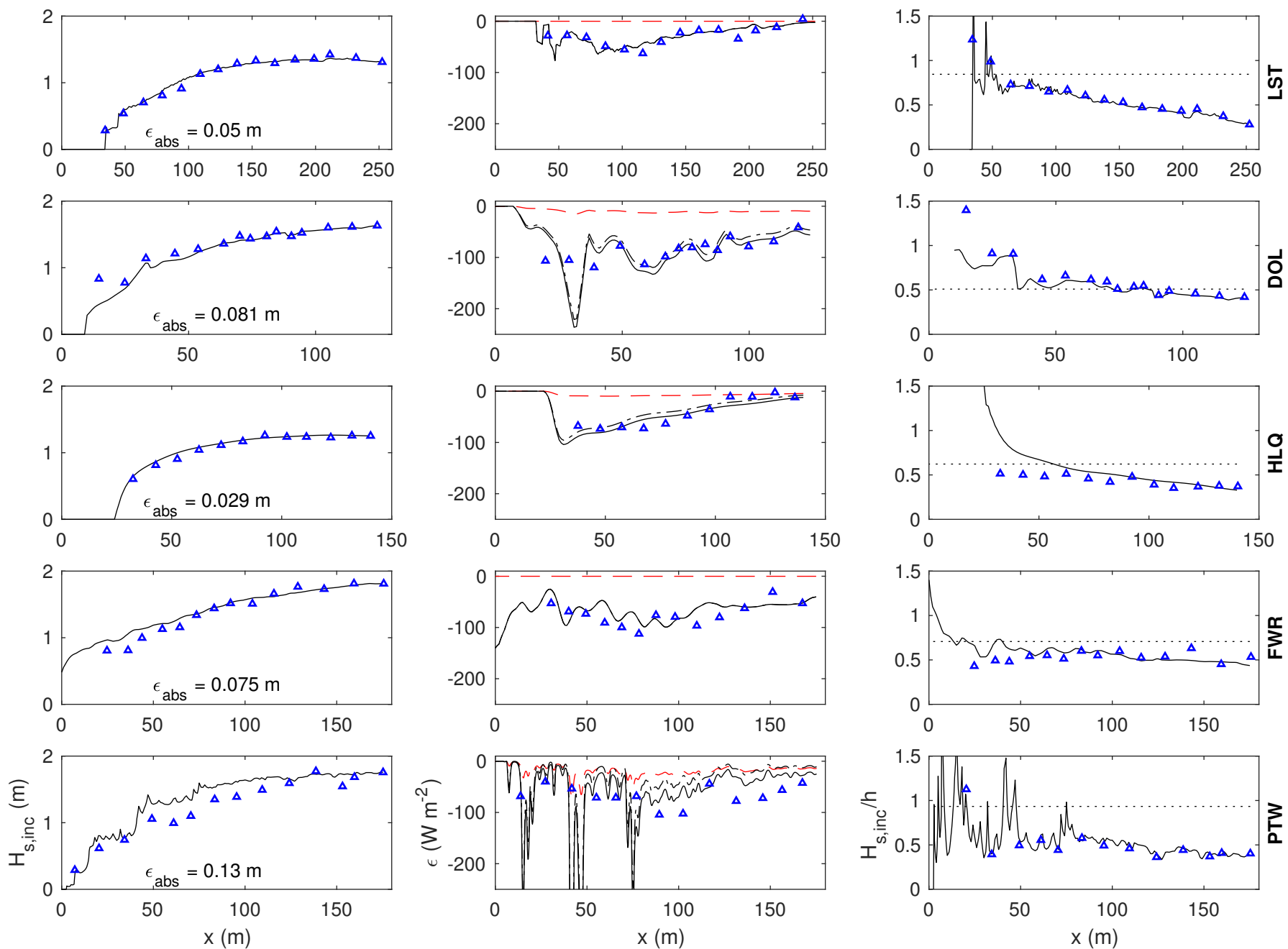


Figure 17.

